

Distribution Agreement

In presenting this thesis as a partial fulfillment of the requirements for a degree from Emory University, I hereby grant to Emory University and its agents the non-exclusive license to archive, make accessible, and display my thesis in whole or in part in all forms of media, now or hereafter now, including display on the World Wide Web. I understand that I may select some access restrictions as part of the online submission of this thesis. I retain all ownership rights to the copyright of the thesis. I also retain the right to use in future works (such as articles or books) all or part of this thesis.

Ciarra Coston

April 10, 2024

Characterizing Habitable Worlds Observatory Targets with TESS: Rotation Periods and
Gyrochronological Age

by

Ciarra Coston

Dr. Alissa Bans
Adviser

Department of Physics

Dr. Alissa Bans
Advisor

Dr. Merida Batiste
Committee Member

Dr. Erin Bonning
Committee Member

2024

Characterizing Habitable Worlds Observatory Targets with TESS: Rotation Periods and
Gyrochronological Age

By

Ciarra Coston

Dr. Alissa Bans

Adviser

An abstract of
a thesis submitted to the Faculty of Emory College of Arts and Sciences
of Emory University in partial fulfillment
of the requirements of the degree of
Bachelor of Science with Honors

Department of Physics

2024

Abstract

Characterizing Habitable Worlds Observatory Targets with TESS: Rotation Periods and Gyrochronological Age

By Ciarra Coston

The Astro 2020 Decadal Survey has recommended that NASA begin to design a 6-meter-class UV/vis/IR space observatory (dubbed Habitable Worlds Observatory, HWO) capable of imaging and spectrally characterizing potentially habitable exoplanets. HWO is slated to launch in the early 2040s and will target small, temperate exoplanets in the habitable zones of approximately 100 bright, nearby, Sun-like stars. To facilitate HWO precursor science efforts by the community, Mamajek & Stapelfeldt (2023) recently compiled the NASA ExEP Mission Star List for the Habitable Worlds Observatory of 164 candidate target stars. We analyzed time-series photometry from NASA's TESS mission to determine the rotation of the stars, and therefore determine gyrochronological ages for these Sun-like stars. We report the measurement of TESS rotation periods for 35 of the HWO ExEP target stars and estimates of gyrochronological ages for 20 of these stars. The ages for these stars range from 99 to 1527 Myr. The results were unsurprisingly biased towards the youngest, most active stars in the sample. Therefore, the future goals are to find longer rotation periods leading to older stars.

Characterizing Habitable Worlds Observatory Targets with TESS: Rotation Periods and
Gyrochronological Age

By

Ciarra Coston

Dr. Alissa Bans

Adviser

A thesis submitted to the Faculty of Emory College of Arts and Sciences
of Emory University in partial fulfillment
of the requirements of the degree of
Bachelor of Science with Honors

Department of Physics

2024

Acknowledgements

I would like to express my deepest gratitude and appreciation to everyone who has contributed to the completion of my undergraduate thesis. Without their support, guidance, and encouragement, this work would not have been possible.

First and foremost, I would like to thank my thesis advisors, Dr. Eric Mamajek and Dr. Emily Gilbert, for their invaluable guidance, insightful feedback, and unwavering support throughout this journey. Their expertise, patience, and encouragement have been instrumental in shaping my research.

I am also grateful to my thesis committee members, Dr. Alissa Bans, Dr. Merida Batiste, and Dr. Erin Wells, for their valuable feedback and suggestions, which have significantly enriched the content and depth of my thesis.

I would like to extend my heartfelt thanks to my family for their constant love, support, and understanding. Their encouragement and belief in me have been my source of strength throughout my academic journey.

I am also thankful to my friends for their encouragement and moral support. Their friendship has made the challenges of this thesis more manageable and the successes more enjoyable.

Thank you once again to everyone who has been a part of this journey and has contributed in any way, big or small. Your support has been invaluable, and I am deeply grateful for it.

This research was carried out in part at the Jet Propulsion Laboratory, California Institute of Technology, under a contract with the National Aeronautics and Space Administration (80NM0018D0004). CC, EG, and EM were supported through the NASA Exoplanet Exploration Program. This research has made use of the NASA Exoplanet Archive, which is operated by the California Institute of Technology, under contract with the National Aeronautics and Space Administration under the Exoplanet Exploration Program. This research has made use of the SIMBAD database, operated at CDS, Strasbourg, France.

Contents

1	Introduction	1
1.1	Exoplanet Detection	1
1.2	Selecting Stars	3
1.3	Gyrochronolgy	5
2	Data	8
2.1	HWO Target Stars	8
2.2	TESS Data	10
2.3	Issues with Data	11
3	Analysis	16
3.1	Periodogram Analysis	16
3.2	Autocorrelation Analysis	18
3.3	Additional Attempted Analysis Methods	20
3.4	Comparison of Measured Rotation Periods to Published Values	22
3.5	Estimating Gyrochronological Ages	23
3.6	Results	25
4	Discussion And Future Work	28
4.1	Discussion	28
4.2	Future Work	29
4.3	Conclusion	29
	References	31
5	Tables	36

List of Figures

1.1	Hertzsprung-Russell (H-R) diagram illustrating the distribution of stars based on their luminosity (in relation to the Sun), surface temperature (in Kelvin) and stellar type. (European Southern Observatory, 2007)	4
1.2	Hertzsprung-Russell (H-R) diagram illustrating the distribution of target stars selected for the project. These stars, resembling our Sun in characteristics, are categorized based on their luminosity and effective temperature. They correspond to the main sequence stars colored from white to red in Figure 1.1.	5
1.3	Example light curve depicting the sinusoidal pattern observed in the flux variations of TIC 381949122 (Zeta Doradus) during sector 62 of the TESS mission. This sinusoidal pattern sine wave shows the movement of sunspots across the star’s surface.	7
2.1	Distance versus luminosity for the target stars. Tier A, B, and C represent different qualities of the targets. Tier A is the best, Tier B is the next level below and Tier C is the lowest quality. The red ‘x’ represents targets that were categorized but ultimately were not selected. (Mamajek & Stapelfeldt 2023)	9
2.2	Light curve of TIC 166646191 observed during sector 48, with vertical green lines overlaid to indicate the occurrences of momentum dumps. Data points affected by momentum dumps are often flagged and removed. In this particular case, we observed peculiar jumps in flux at the second momentum dump, as well as an unrealistic decrease in flux approaching the third momentum dump.	11

2.3	Light curve for TIC 38511251 in two different sectors. More commonly known as Dela Eridani which has a published rotation period of 158 days (Hempelmann 2016)	13
2.4	An example of a light curve of TIC 381949122 using ASAS-SN data in two different magnitudes. This is the same target as demonstrated in 1.3. The difference between the two magnitudes lies in the wavelengths they capture, with V-band encompassing a broader range of visible light and G-band focusing more on the green portion of the spectrum.	15
3.1	Example periodogram illustrating the presence of a prominent peak at a period of 3.4 days. This demonstrates the potential rotation period for the target star, TIC 381949122. This is the same target as Figure 1.3 but for a different sector.	17
3.2	Figure showing the analysis of the light curve for Zeta Doradus (TIC 381949122) from sector 11 of TESS observations. (Top) Light curve displaying the flux variation over time. (Middle) Periodogram revealing peaks indicative of a potential rotation period of approximately 1.75 days. (Bottom) Model fit of the proposed rotation period overlaid on the original light curve.	18
3.3	Autocorrelation function (ACF) analysis performed on target, TIC 381949122 in just sector 11. The resulting average rotation period is 3.425 days, with an error margin of 0.014 days. Parabolas were fitted around each of the peaks (highlighted in red) to evaluate the rotation period associated with the location of the peak vertex.	20
3.4	Autocorrelation function (ACF) analysis performed on target, TIC 381949122 using all 35 sectors the target was present in. The resulting average rotation period is 3.492 days, with an error margin of 0.006 days. Again parabolas were fitted around each of the peaks (highlighted in red) to evaluate the rotation period associated with the location of the peak vertex.	21
3.5	Comparison plot illustrating the correspondence between rotation periods found using periodogram analysis and autocorrelation function (ACF) analysis for the same set of stars. Each point on the plot represents a star's rotation period.	22

LIST OF FIGURES

3.6	Comparison of the rotation periods measured in this project to those previously published in the literature for the same set of stars. The black line represents the two periods equal to each other. The red lines represent the measured period with half or double that of published values.	23
3.7	Scatter plot showing the relationship between rotation period and effective temperature for the analyzed target stars.	26
3.8	Scatter plot showing the relationship between gyrochronology ages and effective temperature for the analyzed target stars.	26

List of Tables

2.1	Breakdown of spectral types and tier for target list	10
3.1	Gyrochronology Ages for HWO Target Stars	24
3.2	Summary of key outcomes of the project, including the number of target stars with data, the rotation periods measured, and gyrochronological ages estimated.	25
5.1	Published Rotation Periods for HWO Target Stars.	36
5.1	(1) Baliunas et al. [9], (2) Baliunas et al. [10], (3) Bazot et al. [15], (4) DeWarf et al. [16], (5) Donahue et al. [11], (6) Dumusque et al. [14], (7) Egeland et al. [12], (8) Fetherolf et al. [13], (9) Gaidos et al. [17], (10) Hempelmann et al. [7], (11) Hempelmann et al. [7], (12) Hempelmann et al. [7], (13) Henry et al. [18], (14) Noyes et al. [8], (15) Schmitt and Mittag [6], (16) Suárez Mascareño et al. [19], (17) Torres and Ferraz Mello [20], (18) Watson et al. [21], (19) Wright et al. [22].	40
5.2	Input Catalog of HWO Target Stars	41

Chapter 1

Introduction

1.1 Exoplanet Detection

One of the most compelling endeavors in astronomy is the study of exoplanets, planets orbiting stars outside of our solar system. The first exoplanet was discovered in 1992. 4,000 planets were found by 2019. As of March 12th, 2024, 5,599 exoplanets have been confirmed. As we continue to study these distant worlds our understanding of the fundamental principles of planetary formation, planetary evolution, and life beyond Earth grows.

Currently, there are four main techniques used to analyze and find exoplanets; radial velocity, transit, direct imaging, and gravitational microlensing. Radial velocity looks for the gravitational tug on a star by its exoplanet (Bozza et al. 2016). The transit method watches for decreases in a star's brightness when a planet passes directly between the star and an observer (Perryman 2018). Gravitational microlensing studies the gravitational forces of very distant objects to bend the light coming from a star (Perryman 2018).

The search for Earth-like exoplanets, particularly through current detection methods, presents significant challenges due to the limitations of the techniques. Gravitational microlensing is very uncommon and does not have any follow-up. The transit and radial velocity methods are highly effective in detecting large exoplanets or those in close orbits around their host stars, but they struggle to detect Earth-sized planets in the habitable zone (Bozza et al. 2016). Since Earth is the only location where we know life can exist, we are specifically looking for similar systems. Hence scientists are looking more into direct imaging to find habitable worlds.

Direct imaging involves capturing the light emitted by an exoplanet. However, the challenge lies in the fact a host star is millions (sometimes billions) of times brighter than the planet. Therefore any light reflected off the planet is drowned out by the star's luminosity. To reduce this issue, various techniques have been developed. The primary techniques include coronagraphs, integrated with a telescope, and starshades, which are independent spacecraft. Both techniques focus on blocking the light from the star. This technique is best for the study of young, massive planets that are far from their host stars. By directly imaging these exoplanets, scientists gain insights into an exoplanet's atmospheric and surface characteristics, and orbital dynamics.

While direct imaging offers a promising approach to identifying distant planets, it remains a laborious and time-intensive process. Directly imaging Earth-like planets requires advanced instrumentation and extensive observation time, making it impractical for large-scale surveys. The exoplanets studied with this method need to be bright and far from their host star. The goal of this project is to provide precursor science specifically to aid in future observatories using the direct imaging method to observe terrestrial-age planets.

The Decadal Survey on Astronomy and Astrophysics serves as a foundational document that guides the direction of astronomical research and exploration over a decade-long period. The survey identifies pressing scientific questions, highlights emerging technologies, and proposes ambitious missions and projects addressing forefront challenges in studying the cosmos. A central theme of the 2020s decadal survey (National Academies of Sciences, Engineering, and Medicine 2023) emphasizes the importance of advancing observations of exoplanets and their host stars. This theme focuses on the community's efforts to deepen our understanding of these systems' formations, evolution, and relationships, while also exploring their potential habitability. To further these goals, the survey recommends the development of a new mission, tentatively named the Habitable Worlds Observatory.

The primary objective of this project is to characterize the potential target stars of the upcoming Habitable Worlds Observatory (HWO). The HWO will be a future NASA space telescope equipped with a 6-meter UV/visible/near-IR capability, anticipated to launch in the early 2040s (National Academies of Sciences, Engineering, and Medicine 2023). Its key capability will be the imaging of Earth-like exoplanets orbiting very nearby, bright,

Sun-like stars. NASA has a primary interest in characterizing potential target stars of HWO to inform the design of the observatory in the next half decade (“precursor science”) and a long-term interest in refining the target list and improving our knowledge of the stars to increase the science return of the mission (“preparatory science”).

1.2 Selecting Stars

Given the limitation of stars and planets HWO can survey, the overall goal of this project is to provide the community with the best stellar targets for future exoplanet surveys. Currently, there is a list of 164 potential targets (Mamajek & Stapelfeldt 2023). Each was chosen based on specific criteria to be considered for this list of precursor stars. The criteria are explained in more depth in section 2.1.

To study the target list, we utilize current data from the Transiting Exoplanet Survey Satellite mission (TESS). TESS, launched in 2018, is an all-sky survey designed to discover transiting exoplanets (Ricker et al. 2014). TESS conducts its survey by systematically scanning broad sectors of the celestial sphere, capturing photometric data from stars within its field of view. Each sector is a designated portion of the sky, spanning 24° by 96° made up of four cameras, that observe continuously for approximately 27 days, before transitioning to the next sector. The satellite is pointed along a line of ecliptic longitude, this allows the satellite to maintain continuous observation of a 24° diameter region centered at one of the ecliptic poles throughout its years-long mission. By alternately focusing on different hemispheres each year, TESS ensures complete coverage of both the northern and southern celestial hemispheres. Currently, TESS continues its data collection across the entire celestial sphere, with ongoing efforts to enhance the coverage of previously surveyed sectors and to refine data for the objects within the ecliptic plane.

To better understand the target list, we first need to understand the foundation of stellar classification. Direct imaging also depends on our ability to characterize the host star of the exoplanet. Stellar classification provides a framework for understanding the properties and behavior of stars. Astronomers use the Hertzsprung-Russell (H-R) diagram as the main means to classify stars. The diagram shows the correlation between a star’s luminosity and its temperature, and spectral type.

The H-R diagram is split into distinct regions based on their characteristics; main

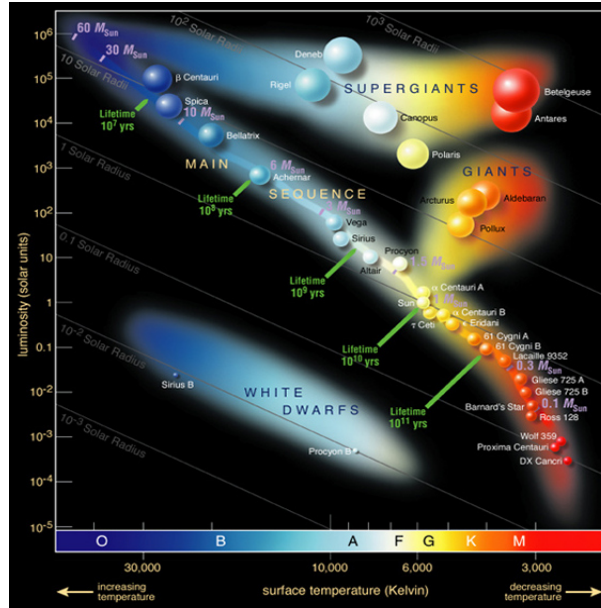


Figure 1.1 Hertzsprung-Russell (H-R) diagram illustrating the distribution of stars based on their luminosity (in relation to the Sun), surface temperature (in Kelvin) and stellar type. (European Southern Observatory, 2007)

sequence stars, giant stars, supergiant stars, and white dwarfs. Main sequence stars, for instance, occupy a diagonal line running from the top left (high luminosity, high temperature) to the bottom right (low luminosity, low temperature) of Figure 1.1. These stars, including our Sun, represent the most common and stable stage of stellar evolution. Giant and supergiant stars, on the other hand, are found in the upper right portion of Figure 1.1. characterized by high luminosity but relatively low surface temperatures. These stars have exhausted their core hydrogen and are in the later stages of stellar evolution. White dwarfs are the remnants of low to medium-mass stars, like the Sun. They appear as faint, hot points on the lower left of Figure 1.1. They are the final evolutionary stage for low to medium-mass stars.

Given our specific interest in identifying exoplanets conducive to life, our search strategy will prioritize locating systems akin to that of Earth—the sole known habitat supporting life. Hence, our focus will be on stars resembling our Sun, classified as G-type stars, as depicted in Figure 1.2.

Thus the targets focus on stars near the G-type stars on the H-R diagram. F/G/K-type stars are generally considered “Sun-like” as they have similar masses, effective temperatures, interior structures, and activity/rotation evolution.

Understanding the properties of these stars, such as their mass, temperature, and

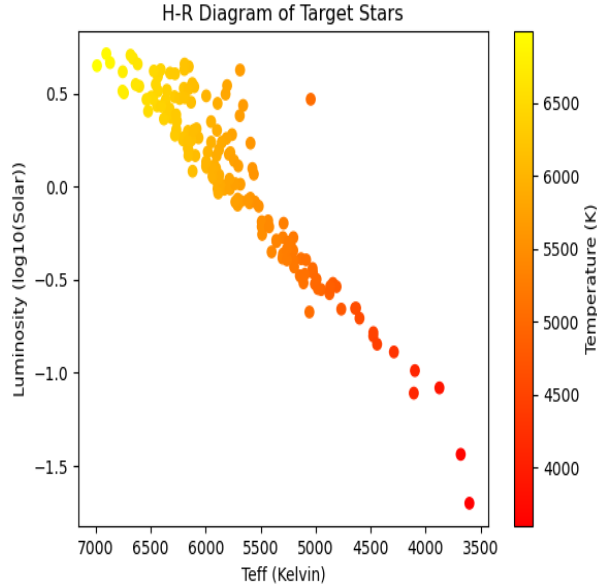


Figure 1.2 Hertzsprung-Russell (H-R) diagram illustrating the distribution of target stars selected for the project. These stars, resembling our Sun in characteristics, are categorized based on their luminosity and effective temperature. They correspond to the main sequence stars colored from white to red in Figure 1.1.

age, provides essential context for interpreting the observations of the host’s exoplanets. Furthermore, the study of host stars increases the understanding of stellar evolution in conjunction with planetary systems.

1.3 Gyrochronology

Age-dating host stars play a pivotal role in describing a planetary system. The age of a host star influences its composition and dynamic, both of which affect the potential habitability of any orbiting exoplanets. For instance, younger stars tend to exhibit higher activity levels, such as stellar flares, which can render closely orbiting planets uninhabitable (Perryman 2018). Therefore, we aimed to identify stars with smoother, slower rotations, as they are more likely to host planetary systems conducive to habitability. This report focuses on the process of age-dating a list of target stars, by utilizing gyrochronology.

Gyrochronology operates on the premise that stars gradually reduce their rotation speed as they age due to the loss of angular momentum. Sun-like stars are born fast rotating (period ≤ 1 week) and gradually slow down over time to periods of weeks to months, primarily through magnetic braking (Perryman 2018). Sun-like stars have ion-

ized convective envelopes, which are the outer layers of a star, that transport energy via convection driven by temperature differences, and differential rotation, meaning that various parts of the star rotate at varying speeds. These two processes combine to generate magnetic fields that extend beyond the stellar surface. Stellar winds launch ionized materials into these magnetic fields. The magnetic fields capture the materials which then rotate at the star's angular velocity before being expelled into space. This effect carries away mass from the star, thus removing angular momentum from the star and gradually decelerating its rotation over time.

Gyrochronology is an empirical means of estimating stellar ages using their rotation periods. To calculate the gyrochronal ages we utilized the work of Bouma et al. (2023) who provided an updated temperature-rotation-age relation for low-mass stars. This updated relation was calibrated by age-dated star clusters. The authors developed the Python model, `gyrointerp`, which effectively models the evolution of rotation periods for stars on the main sequence with temperatures ranging from 3800 to 6200 K (masses of 0.5-1.2 M_{\odot}). To utilize this model, we found the rotation periods of the target stars.

The rotation period of a star can be determined by observing the periodic changes in its brightness (or flux) over time. These changes are closely associated with the star's magnetic activity, which gives rise to the formation of dark spots on its surface (Perryman 2018). These dark spots are notably cooler than the surrounding areas which leads to fluctuations in the star's flux. As a dark spot comes into view of the telescope, it causes a decrease in the overall flux, resulting in a dip in brightness. Conversely, when the spot is not visible, the flux returns to its regular level. The recurrent changes in flux as the star rotates provide the information needed to find the rotation period. This process is typically graphically represented as a light curve. Where time is plotted on the horizontal axis and flux on the vertical axis as shown in Figure 1.3. Overall this process is referred to as time-series photometry.

To complete the analysis, two Python packages were utilized; `Lightkurve` (Lightkurve Collaboration et al 2018) and `SpinSpotter` (Holcomb et al. 2022). `Lightkurve` is an open-source Python package specifically designed to manipulate astronomical time series data, from Kepler and TESS. `SpinSpotter` was developed by Rae J. Holcomb, Paul Robertson, Patrick Hartigan, et al. It's an automated algorithm designed to utilize auto-correlation functions to identify stellar rotation periods. The in-depth analysis conducted

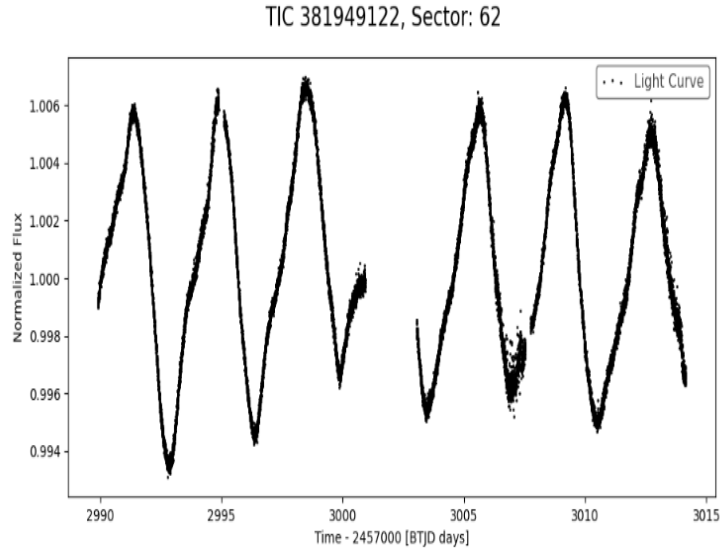


Figure 1.3 Example light curve depicting the sinusoidal pattern observed in the flux variations of TIC 381949122 (Zeta Doradus) during sector 62 of the TESS mission. This sinusoidal pattern sine wave shows the movement of sunspots across the star’s surface.

using these two programs is explained in section 3.

In this project, I aimed to use time-series photometry to determine to gyrochronologically age date Sun-like stars with currently available data, thus contributing to the ongoing precursor science around HWO. This thesis is divided into four main sections: Data, Analysis, Discussion and Future Work, and Conclusions. The Data section presents the datasets used in the project and discusses their respective issues. In the Analysis section, the methodology for determining rotation periods and ages is explained, along with the final results. The Discussion and Future Work section explores the implications and limitations of the findings and outlines potential areas for further investigation. Finally, the Conclusions section offers concluding remarks and summarizes the key findings of the thesis.

Chapter 2

Data

2.1 HWO Target Stars

As mentioned above, the Habitable Worlds Observatory (HWO) is limited in the number of stars and planets it can survey. Therefore, the main goal was to identify and present the scientific community with the most promising stellar candidates for future exoplanet surveys. Eric Mamajek and Karl Stapelfeldt created a list of 164 potential targets for this purpose (Mamajek & Stapelfeldt 2023). To omit undesirable targets, two main limitations were placed on the target stars. The stars all must have a habitable zone that will be accessible to view in the UV/visible/near-infrared with a combination of a 6-meter mirror and a starlight suppression technology (either a coronagraph or starshade). Direct imaging of Earth-like planets is limited to the brightness of their host. Hence, the inner working angle was the first factor taken into account when creating this target list. The inner working angle (IWA) is approximately the smallest apparent separation between a planet and its host at which the planet is detectable. In exoplanet imaging, the IWA determines the minimum distance between a planet and a star at which a telescope can detect the planet without being overwhelmed by the star's brightness. The targets were chosen if they have an angular separation that falls outside of the IWA of the potential HWO coronagraph. Secondly, to avoid long exposure times to detect planets in reflected light, an apparent magnitude limit was placed on the targets as well. Apparent magnitude refers to the measure of the brightness of a star as seen from Earth. Lower magnitudes indicate brighter stars and higher magnitudes represent dimmer ones. In addition to these two main factors, an exoplanet brightness limit, exoplanet-star brightness ratio

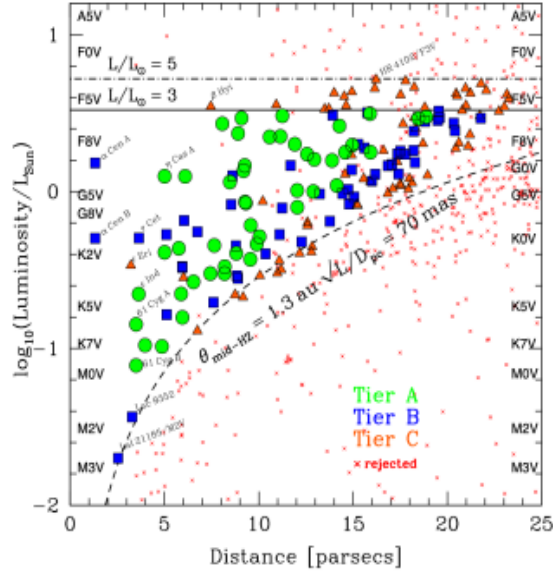


Figure 2.1 Distance versus luminosity for the target stars. Tier A, B, and C represent different qualities of the targets. Tier A is the best, Tier B is the next level below and Tier C is the lowest quality. The red ‘x’ represents targets that were categorized but ultimately were not selected. (Mamajek & Stapelfeldt 2023)

limit, the presence of a circumstellar disk, and an assessment of the stellar multiplicity of the system have characterized each target.

The targets were split into three tiers; A, B, and C. The relationship between target luminosity, distance, and tier can be seen in Figure 2.1. Tier A was considered the best, and tier C was a lower quality while tier B was in between the other two. Targets in tier A have an IWA of 83 milli-arcseconds (mas). Targets in Tier B have an IWA of between 72 mas and 83 mas while Tier C has an IWA of 65 mas and 72 mas. Along with the limits placed on the IWA, the planet-star brightness ratios, distance between planet and host, the presence of an optically thin cold disk, or the presence of a binary also went into their ranking. The total number of stars in each tier is shown in Table 2.1. All the stars were analyzed regardless of tier. For more details on the original target star selection, see the NASA ExEP Mission Star List for the Habitable Worlds Observatory 2023 document by Mamajek & Stapelfeldt (2023).

The HWO target stars primarily belong to the spectral types F, G, and K, with a few early M-type stars. The breakdown of each spectral type per tier is shown in Table 2.1. The F/G/K-type stars are generally considered “Sun-like” as they have similar masses, effective temperatures, interior structures, and activity/rotation evolution to the Sun. They typically exhibit magnitudes brighter than the 6th magnitude except for a few

M dwarfs of the 7th magnitude. Another critical characteristic of these stars is their proximity to Earth, all the target stars are within a distance of 25 parsecs.

Table 2.1: Breakdown of spectral types and tier for target list

	F-type	G-Type	K-Type	M-Type	Totals
Tier A	14	15	17	1	47
Tier B	15	23	11	2	51
Tier C	37	17	12	0	66
Total	66	55	40	3	164

2.2 TESS Data

TESS releases several data products: raw full-frame images, calibrated full-frame images, target pixel files, light curves, flat fields, pixel response functions, and lists of TESS Objects of Interest (TOIs). For about 200,000 target stars, TESS downloads data of the stars in view at a two-minute cadence in small cutaways called ‘postage stamps’. A cadence refers to the frequency at which observations are taken. Hence a two-minute cadence means there are two minutes between successive observations of a target star’s brightness.

We utilize two-minute cadence photometric data, which measures the brightness (or flux) of a star over time. This cadence allows for enough data to view the movement of star spots over time. By observing the repeated fluctuations in flux, we can determine the rotation period of a star.

Since its launch in 2018, many of the targets have been viewed in multiple sectors. All reliable sectors were observed and taken into account when finding a target’s period. The analysis of targets with multiple sectors is further explained in section 3. Currently, there are 77 sectors available for study with an additional six sectors planned for the remainder of the year. However, this project only viewed targets up to sector 72.

The initial step in the analysis involved using Lightkurve to create a scatter plot (or light curve), representing time versus flux, for a target star within a specific TESS sector. This visualization provides a clear representation of the variations in the star’s brightness over time. Because of the periodic movement of the star spots, the light curve is expected to have a sinusoidal pattern which can be seen in Figure 1.3.

2.3 Issues with Data

During this process, we encountered numerous challenges in creating light curves, including missing data, errors stemming from instrumental effects, or limitations imposed by the star's position in the sky.

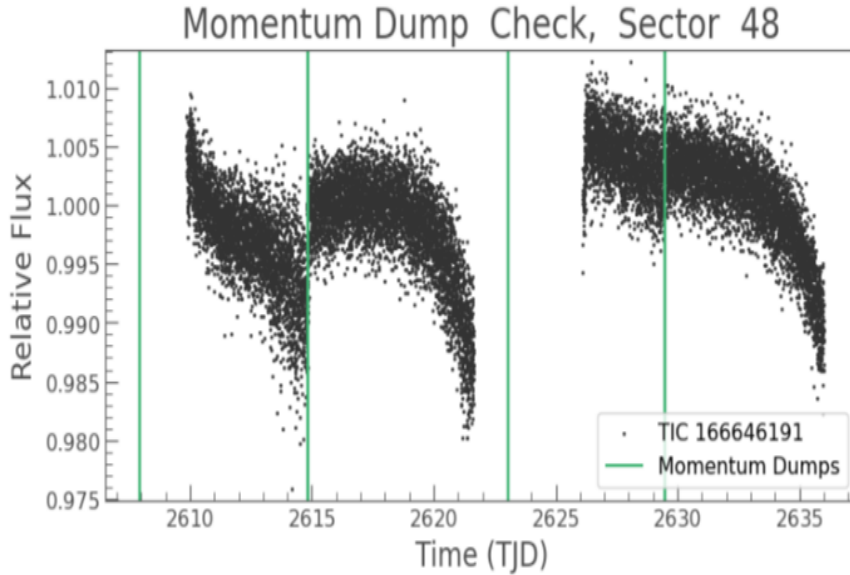


Figure 2.2 Light curve of TIC 166646191 observed during sector 48, with vertical green lines overlaid to indicate the occurrences of momentum dumps. Data points affected by momentum dumps are often flagged and removed. In this particular case, we observed peculiar jumps in flux at the second momentum dump, as well as an unrealistic decrease in flux approaching the third momentum dump.

The most common issues stemmed from instrumental effects such as momentum dumps. Momentum dumps are a consequence of the reaction wheels used to maintain spacecraft pointing. Reaction wheels are used to keep the spacecraft stable and control the position of the spacecraft through an electric motor and the generation of angular momentum to counteract solar radiation pressure. Over time, reaction wheels build up angular momentum, saturate, and need to be reset. Once the wheels saturate and when they are spun down in the reset process, TESS pointing is less stable. This data is often flagged as problematic and removed. Since momentum dumps are conducted at regularly scheduled periodic times, they often show up as false positives in the periodograms. Figure 2.2 illustrates a clear upward jump in flux after the second momentum dump, indicated by the vertical green line. Additionally, a distinct decrease in flux is observable as the data approaches the third momentum dump.

The early sectors are more significantly affected by instrumental effects like momentum dumps, therefore this data is less reliable. For instance, Dela Eridani has a published rotation period of 158 days (Hempelmann 2016). It was initially observed in TESS sector 4, shown in Figure 2.3a, where the flux was sporadic for an object that has a rotation period over five times longer than can be seen in a single TESS sector. In the middle of the light curve, there is a massive spike in flux that does not seem to fit with the surrounding data. As time has passed, the momentum dumps have become less of an obstacle but any outlier light curves were first checked to see if momentum dumps affected the data. Figure 2.3b, shows the same target 27 sectors later. This light curve matches what is expected, i.e. the curve was very smooth and does not show any clear signs of periodicity in the short twenty-seven-day sector.

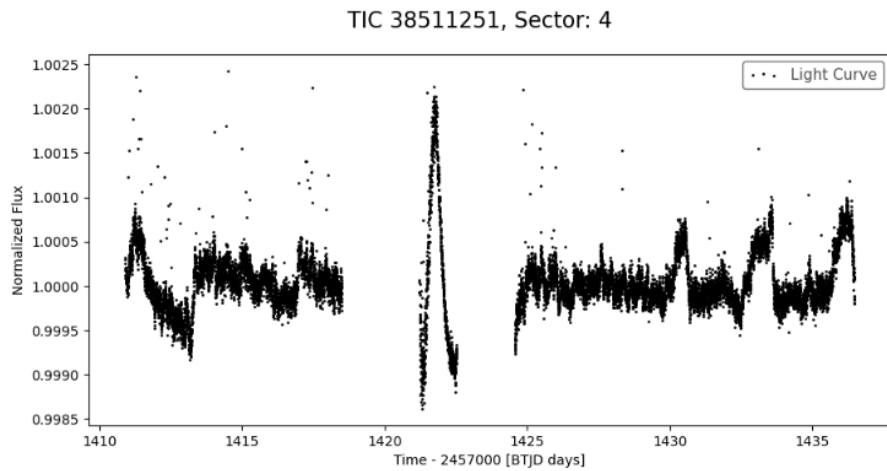
Along with momentum dumps, scattered light from the Moon, Earth, or Sun can often make data unusable. This light may oversaturate the cameras, causing the data to be removed in preprocessing. This was most commonly seen in stars located along the ecliptic; the apparent path of the Sun across the celestial sphere.

The remaining issues stemmed from specific stellar cases. For instance, a few targets had light curves that showed two sinusoidal waves competing with each other. This phenomenon often indicates differential rotation, where different parts of a star rotate at varying speeds, and evolving star spots. Therefore, it becomes challenging to discern which sinusoidal wave accurately represents the star's true period. This case is shown in Figure 3.2.

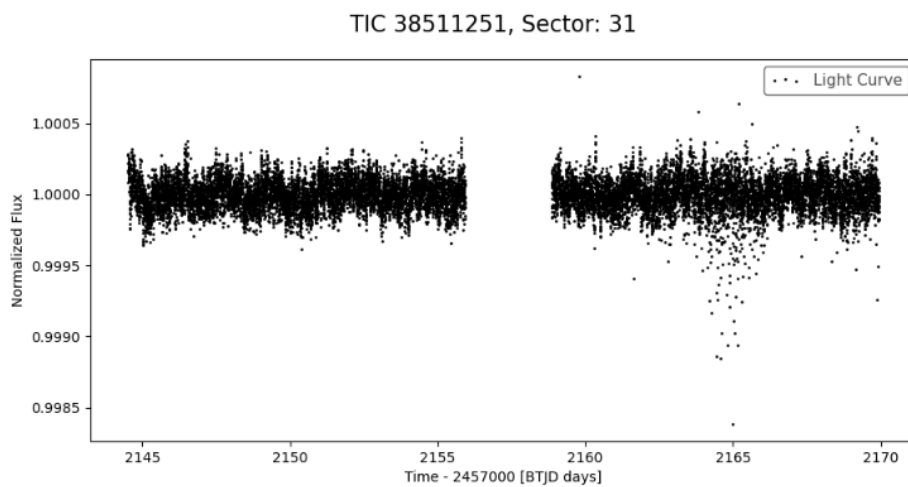
In another scenario, two stars fell within the same pixel, resulting in a combined light curve for both stars that was essentially unusable. While another did not show a single star in the target pixel file.

Overall, many of these issues with the TESS data could not be helped. We would often have to void data from specific sectors due to unreliable data. Many of the targets had only a single unusable sector and at least one other sector to look at.

Other than difficulties in analyzing the light curve, the TESS data had one other major issue. The data spans 27 days which means we can only accurately get periods less than 10 days. As mentioned above faster rotation stars are younger and have higher activity levels which makes them very poor candidates for habitability. Thus the majority of the periods found are short. In order to counter this, we explored the All-Sky Automated



(a) Sector 4, for this target was an unusual light curve for a target known to have a very long rotation period. The changing flux led the analysis methods to give false positives for several rotation periods.



(b) Sector 31, had a light curve that was more likely to match that of the published period. There were still signs of scattered light in the second half of the plot but not enough for the analysis method to have a false positive.

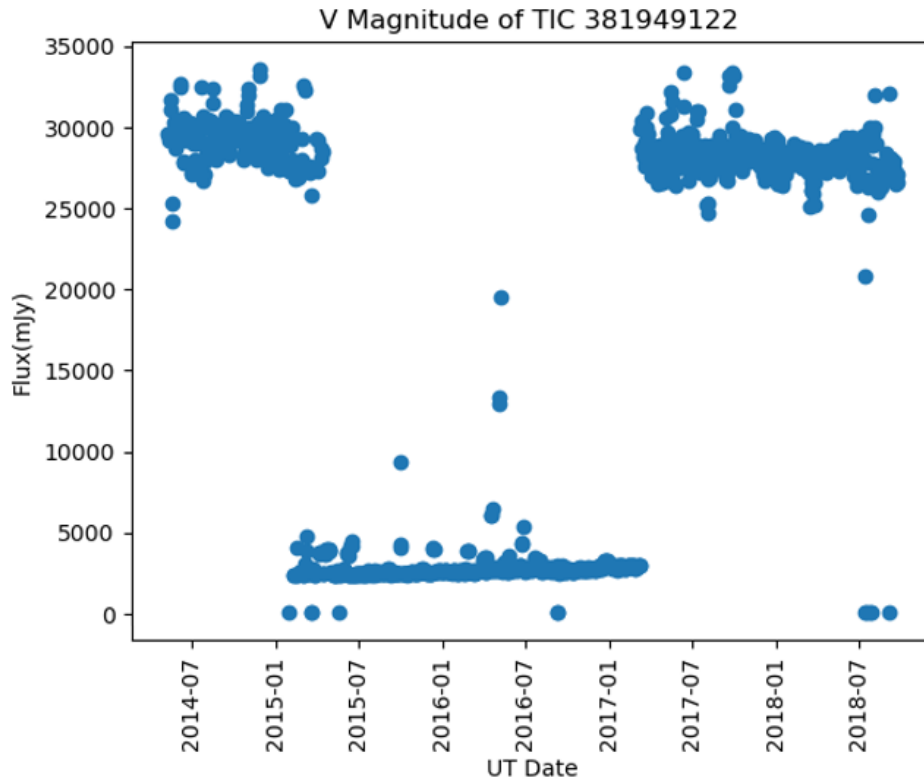
Figure 2.3 Light curve for TIC 38511251 in two different sectors. More commonly known as Dela Eridani which has a published rotation period of 158 days (Hempelmann 2016)

Survey for Supernovae (ASAS-SN) data set.

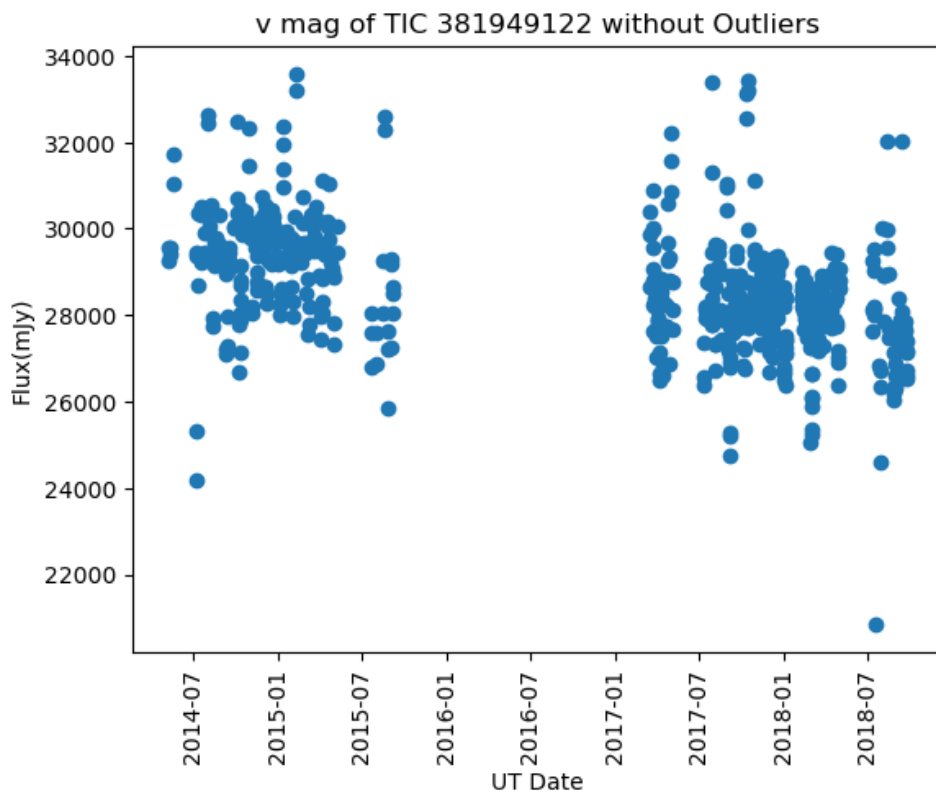
ASAS-SN is comprised of 24 telescopes globally capable of constant photometric observations of the entire visible sky every night (Kochanek et al. 2017). Ideally, ASAS-SN would be able to provide data on our targets for much longer time frames than twenty-seven days. However, this was not the case. Much of the data contained outliers that do not look consistent with astrophysical phenomena and are simultaneously too large to be photometric noise. This is demonstrated in Figure 2.4 which is the same target that will be explored in Section 3.2.

ASAS-SN was originally designed for much fainter objects. It can view objects down to about the 18th magnitude. The dimmest of the stars on the target list has a magnitude of 7 with the major of the targets have a magnitude ranging from 3 to 6. The ASAS-SN data may be a better choice for finding longer periods but, it is not optimal for bright stars. Therefore we did not use any ASAS-SN data in the analysis of the periods for the target star.

The TESS data revealed challenges such as missing data, instrumental effects like momentum dumps, and scattered light interference. Despite these challenges, we were still able to determine periods for many of the targets.



(a) The V-band magnitude measures the brightness of the star in the visible spectrum, specifically in the V or visual band,



(b) The V-ban magnitude without the outliers.

Figure 2.4 An example of a light curve of TIC 381949122 using ASAS-SN data in two different magnitudes. This is the same target as demonstrated in 1.3. The difference between the two magnitudes lies in the wavelengths they capture, with V-band encompassing a broader range of visible light and G-band focusing more on the green portion of the spectrum.

Chapter 3

Analysis

3.1 Periodogram Analysis

To analyze the TESS data the Python package `Lightkurve` was used. The initial step in the analysis involves using `Lightkurve` to create a scatter plot (or light curve), representing time versus flux, for a target star within a specific TESS sector. Since all of the targets were very bright, we could analyze the raw data from every sector a target was present in. This visualization provides a clear representation of the variations in the star's brightness over time. From here we can use the `Lightkurve` package to create a periodogram of the time series data. Essentially, a periodogram measures the strength of periodic signals across a range of frequencies. The highest peak (high power) of the periodogram presents a high likelihood of that being the period of the data. Smaller peaks (low power) are often present in the periodogram, many of them are aliased or caused by other effects in the light curve. To mitigate such potential false factors, a maximum possible period of 30 days is set for the periodogram. This decision is based on the fact that a single TESS sector, spanning 27 days, would not contain sufficient data to observe more than two complete rotations of a star with a period longer than 13 days.

The `Lightkurve` package creates the periodogram based on the Lomb-Scargle model. A Lomb-Scargle model is a well-known method that is used for detecting periodicity in time series. The Lomb-Scargle model overcomes the limitations of traditional Fourier analysis by identifying periodic variations in time-series data with uneven time sampling. The algorithm fits a sinusoidal model to the time-series data, varying the frequency of the sinusoidal function and calculating the fit at each frequency point.

3.1 Periodogram Analysis

The model measures the strength of the periodic signal at each frequency by quantifying the comparison between the sinusoidal model and the observed data. This results in a periodogram that plots the power of periodic signals against their corresponding frequencies. Higher peaks in the periodogram indicate the presence of strong periodic signals at those particular frequencies. For this project, the periodogram showed the highest peaks on the most likely time (in days) it takes for the star to complete a single rotation. Figure 3.1 has the highest power at 3.4 days hence this star has a period of 3.4 days.

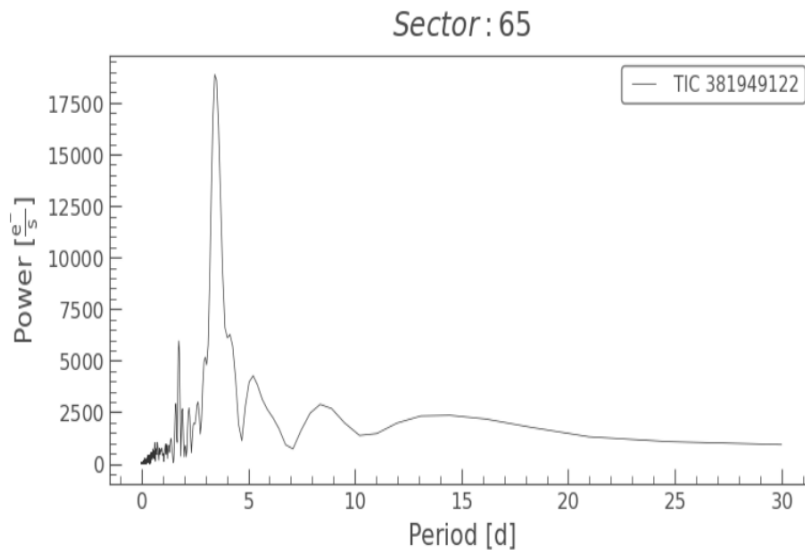


Figure 3.1 Example periodogram illustrating the presence of a prominent peak at a period of 3.4 days. This demonstrates the potential rotation period for the target star, TIC 381949122. This is the same target as Figure 1.3 but for a different sector.

As mentioned above many of the targets have data in multiple TESS sectors. Each sector was taken into account for finding the period for each target. A period was found for every reliable sector, and all of those periods were then averaged together to get the best overall period. An uncertainty value was calculated by the standard deviation. Each target had its own special circumstances, therefore more specific information is within the final table.

3.2 Autocorrelation Analysis

Autocorrelation analysis is another technique used in the examination of time series data, providing insights into the relationships between sequential observations within the data set. Autocorrelation works by investigating how each data point in a time series relates to its preceding data points, known as lags. It aims to quantify the correlation between observations at different time points within the same data set. This analysis helps unveil underlying trends that exist within the time series.

Periodograms are more sensitive to noise and outliers, which can obscure or distort the periodic signals. This leads the periodogram to produce false peaks, especially with sparse or irregularly sampled data. This problem was most often seen in stars with differentiating or evolving star spots.

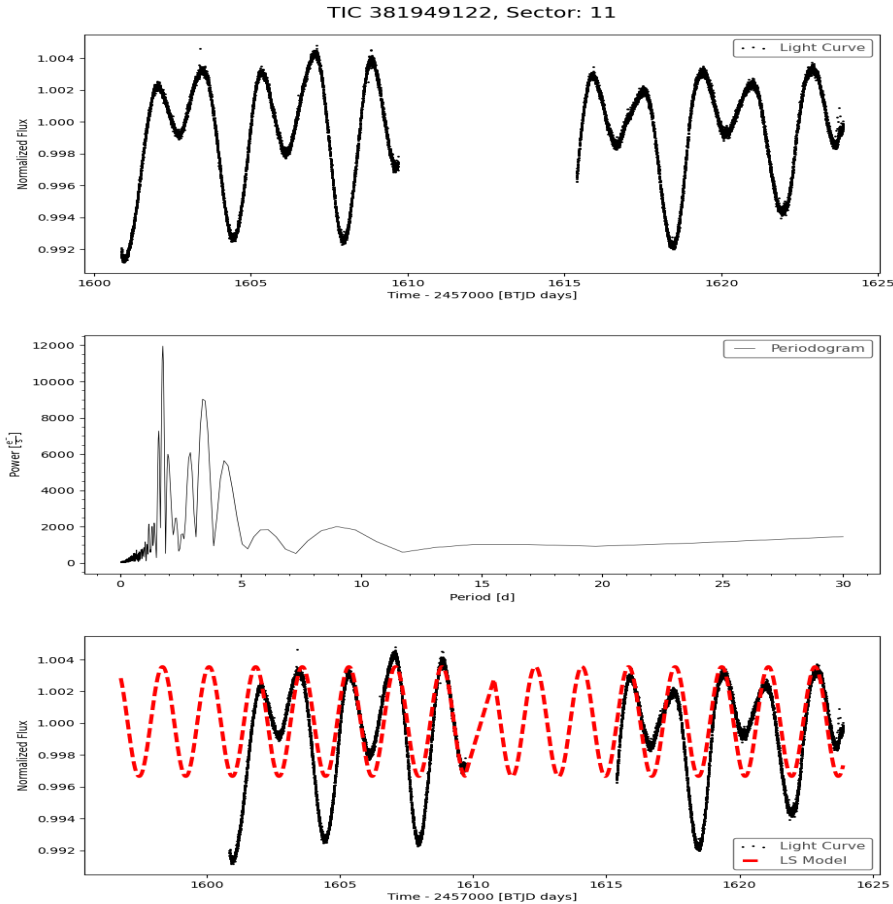


Figure 3.2 Figure showing the analysis of the light curve for Zeta Doradus (TIC 381949122) from sector 11 of TESS observations. (Top) Light curve displaying the flux variation over time. (Middle) Periodogram revealing peaks indicative of a potential rotation period of approximately 1.75 days. (Bottom) Model fit of the proposed rotation period overlaid on the original light curve.

For example, let's examine the star Zeta Doradus (TIC 381949122). Zeta Doradus is both hotter and brighter than the Sun, and lies close to the southern ecliptic, placing it in Tess's southern continuous view zone. Consequently, there are 35 sectors of data available for this star. However, for the purpose of this example let us assume we only have sector 11. Figure 3.2 shows the light curve, the periodogram, and a model depicting the predicted rotation period overlaid on the original light curve. Visually we can see a reoccurring M-shaped pattern in the top plot of figure 3.2. This pattern likely arises from star spots in the opposite hemispheres of the star, resulting in alias peaks at half of the true rotation period. The periodogram struggles to constantly and accurately distinguish such stellar phenomena. In the middle plot of Figure 3.2, another peak appears with high power at approximately double the first one. In this sector, this second peak seems to make more sense, corresponding to the more significant recurring decrease of flux. Additionally, we know that a period of 1.75 days is incorrect because of the vast amount of sectors that this target was viewed in. Over time we can see how the spots evolve; some sectors show the spots perfectly in sync, while others exhibit the opposite behavior. However, this is not the case for most of the targets. Therefore, we turn to autocorrelation for a more robust defense against noise and outliers.

The Python package `SpinSpotter` was used to perform an autocorrelation analysis on the targets (Holcomb et al. 2022). `SpinSpotter` starts by normalizing each sector before stitching them all together into a single multi-sector light curve. The next step calculates the autocorrelation function of that multi-sector light curve and generates an initial estimate for a rotation period. This estimate was then compared to the light curve to ascertain various parameters describing the fit.

Let's revisit the example of Zeta Doradus. When we analyze only sector 11 of Zeta Doradus using `SpinSpotter`, we obtain the plot depicted in Figure 3.3, along with a period of 3.425 ± 0.014 days, which closely aligns with periods found in other sectors. `SpinSpotter` was able to return a more accurate period but it is worth noting that the wave in Figure 3.3 is not the typical sinusoidal wave we would expect. This discrepancy arises because the autocorrelation function bases its findings solely on the provided data. When we augment the autocorrelation function with additional data to use as lags, we achieve a much smoother result, as demonstrated in Figure 3.4.

Both periodograms and autocorrelation functions are valuable tools for this project.

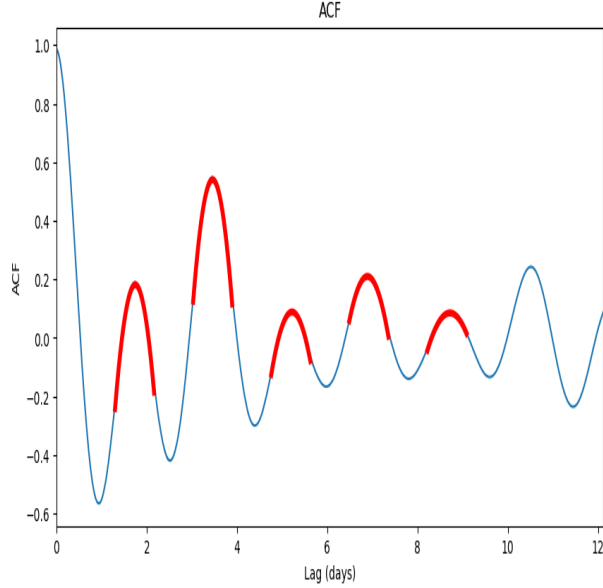


Figure 3.3 Autocorrelation function (ACF) analysis performed on target, TIC 381949122 in just sector 11. The resulting average rotation period is 3.425 days, with an error margin of 0.014 days. Parabolas were fitted around each of the peaks (highlighted in red) to evaluate the rotation period associated with the location of the peak vertex.

While periodograms were useful for identifying sinusoidal periodic signals across a range of frequencies, they often struggled to distinguish complex periodic patterns caused by evolving star spots. On the other hand, autocorrelation functions offer a more robust defense against noise and outliers by directly measuring the similarity between a signal and a time-shifted version of itself. However, they tended to require more data to produce accurate plots. By leveraging the strengths of both methods, we were able to better navigate the challenges posed by noisy or incomplete data.

3.3 Additional Attempted Analysis Methods

In response to problematic sectors and in the hopes of finding accurate periods from stars with periods longer than 13 days, we also tried two other methods.

For the targets with data within several sectors, we looked into combining the light curves into a single plot. The `stitch()` method in the `LightKurve` package allows astronomers to merge TESS target pixel files (TPFs) seamlessly. The method aligns the TPFs' timestamps and combines their pixel values to create a unified dataset covering an extended period of time. Once the combined light curve was generated, we could utilize a periodogram on the new light curve to determine its period. This process helps identify

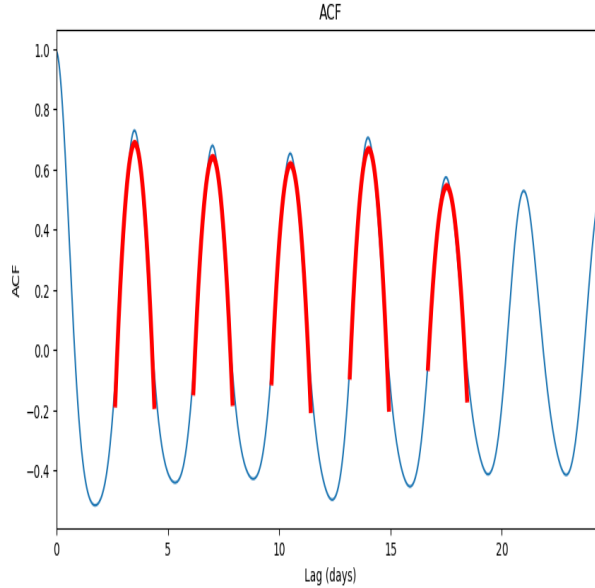


Figure 3.4 Autocorrelation function (ACF) analysis performed on target, TIC 381949122 using all 35 sectors the target was present in. The resulting average rotation period is 3.492 days, with an error margin of 0.006 days. Again parabolas were fitted around each of the peaks (highlighted in red) to evaluate the rotation period associated with the location of the peak vertex.

long-term periodic signals.

This method worked best for targets viewed in consecutive or close to consecutive sectors. In such cases, the periodic signal could be consistently detected across multiple sectors. However, for targets observed in sectors separated by months or even years, stitching the light curve proved to be less effective.

A considerable amount of the combined light curves of multi-sector targets’ periodograms lacked a clear peak, indicating that there was not a dominant periodic signal present in the data. Instead, the power is spread out across a range of frequencies without any distinct maximum. This can happen for various reasons, including random noise in the data, irregular sampling intervals, or the absence of a true periodic signal. In the case of the stitched data of sectors greater than several months, the poor periodic signal was more likely caused by the variability between the sectors. Overall time the spots of stars evolve or the star could be rotating differentially thus causing the light curves to be drastically different over time.

Secondly, we tried the Python package titled `Unpopular` which extracts “de-trended” Full Frame Images (FFI) light curves (Hattori et al. 2021). The FFI’s contain systematic effects, such as scattered light from the Earth and Moon, which need to be removed (“de-

3.4 Comparison of Measured Rotation Periods to Published Values

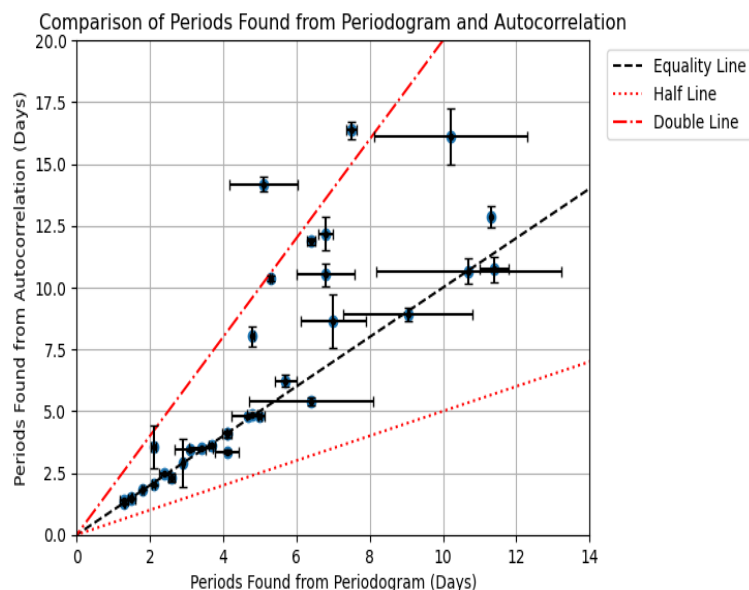


Figure 3.5 Comparison plot illustrating the correspondence between rotation periods found using periodogram analysis and autocorrelation function (ACF) analysis for the same set of stars. Each point on the plot represents a star’s rotation period.

trended”) before any analysis can be done. `Unpopular` effectively removes these common trends by modeling the systematics in a given pixel’s light curve as a linear combination of light curves from numerous other distant pixels on the same CCD detector.

TESS data has its own detrending methods, but their techniques optimize removing data to support exoplanet detection. In contrast, `unpopular`, optimizes variable sources. Thus making it a viable choice for detecting stellar flux changes and identifying rotation periods.

My goal for `unpopular` was to clean up some of the noisier light curves. However, we were unable to get confident results. We often got drastically different periods, for the same target, by slightly changing the parameters of the code. In the end, we decided that this was not the best use of time.

3.4 Comparison of Measured Rotation Periods to Published Values

We possess multiple estimates of the rotation periods, obtained both by sector (for numerous targets) and through different techniques (periodogram vs. autocorrelation). Given that many of the targets are bright naked-eye stars, they have been objects in previous

studies. Consequently, we can cross-reference our measured estimates with those previously published, which have been compiled in Table 5.1. This comparison allows us to validate our findings and confirm the consistency and reliability of our techniques. Additionally, it provides insights into any discrepancies or variations between our results and those reported in the existing literature.

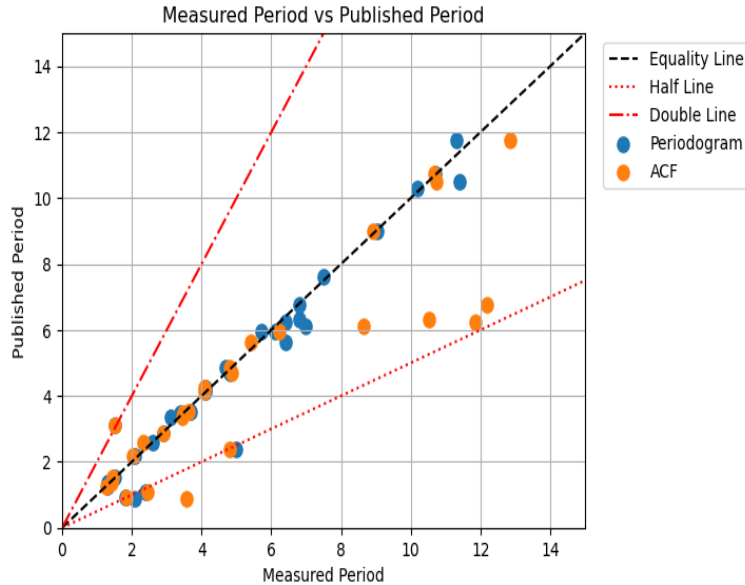


Figure 3.6 Comparison of the rotation periods measured in this project to those previously published in the literature for the same set of stars. The black line represents the two periods equal to each other. The red lines represent the measured period with half or double that of published values.

3.5 Estimating Gyrochronological Ages

After finding as many rotation periods as possible the targets could be age-dated with the Python package `gyrointerp`, the model from Bouma, Palumbo & Hillenbrand (2023). The code can find the age of main-sequence stars with temperatures of 3800-6200 K (masses of 0.5-1.2 M_{\odot}). Which gives ages between 0.08-2.6 Gyr. These limits are based on properties of stellar evolution. The rotation period of younger stars is representative of the stellar age range used for the model. Stars older than the limit are more affected by stellar evolution which causes their rotation periods to change.

One of gyrochronological age dating key strengths is its reliance on observable stellar properties, such as rotation periods, temperature, and color, which can be directly measured from observational data. Preexisting methods for attempting to determine stellar

3.5 Estimating Gyrochronological Ages

Table 3.1: Gyrochronology Ages for HWO Target Stars

TIC ID	HD name	Period (Days)	Period Error	Age	Age Error (+)	Age Error(-)
TIC 421189312	HD 105452 A	3.1	0.430	nan	nan	nan
TIC 441709021	HD 126660 A	2.9	0.020	nan	nan	nan
TIC 229902025	HD 134083	1.5	0.099	nan	nan	nan
TIC 350673608	HD 147513	7.0	0.891	593.99	161.52	130.26
TIC 329574145	HD 165185	5.7	0.292	432.46	78.16	72.95
TIC 238432056	HD 166	6.4	0.114	364.73	72.95	109.42
TIC 30016911	HD 17925	6.8	0.200	265.73	104.21	104.21
TIC 403585118	HD 193664	6.4	1.688	630.46	375.15	270.494
TIC 29495621	HD 199260	4.1	0.004	nan	nan	nan
TIC 88523071	HD 20010 A	4.1	0.140	583.57	281.36	171.94
TIC 343813545	HD 20630	9.04	1.755	807.62	296.99	250.1
TIC 301880196	HD 206860	4.68	0.444	333.47	88.58	93.79
TIC 279649049	HD 20807	5.1	0.936	328.26	130.26	140.68
TIC 97402436	HD 210302	5.0	0.031	nan	nan	nan
TIC 69889261	HD 213845 A	1.3	0.013	nan	nan	nan
TIC 206686962	HD 216803	10.2	2.085	739.88	458.52	406.41
TIC 234968549	HD 219482	2.1	0.035	nan	nan	nan
TIC 118572803	HD 22049	11.3	0.017	1,062.93	83.37	99
TIC 9150015	HD 25457	1.5	0.003	nan	nan	nan
TIC 353257675	HD 25998	2.6	0.086	nan	nan	nan
TIC 117979951	HD 30495	11.4	0.402	1,375.55	171.94	156.31
TIC 399665349	HD 30652	1.8	0.019	nan	nan	nan
TIC 381949122	HD 33262 A	3.4	0.321	375.15	161.52	119.84
TIC 47346402	HD 35296	3.7	0.081	380.36	114.63	93.79
TIC 311063391	HD 37394	10.7	2.518	927.45	380.36	401.2
TIC 93280676	HD 38393	6.8	0.784	nan	nan	nan
TIC 46125330	HD 43042	4.1	0.320	nan	nan	nan
TIC 437886584	HD 43386	2.4	0.157	nan	nan	nan
TIC 282210766	HD 50281	4.8	0.040	99.00	208.42	67.74
TIC 80226651	HD 50692	5.3	0.034	401.20	62.53	62.53
TIC 417762326	HD 72905	4.8	0.143	317.84	67.74	72.95
TIC 181273463	HD 74576	7.5	0.137	244.89	99	83.37
TIC 11310083	HD 84117	6.1	0.766	1,526.65	541.88	521.04
TIC 367631379	HD 90089 A	1.3	0.115	nan	nan	nan
TIC 453620177	HD 90589	2.1	0.076	nan	nan	nan

ages are the isochrone and chromospheric techniques. The isochrone technique involves comparing observed properties of stars, such as luminosity, temperature, and metallicity, to theoretical stellar evolution models represented by isochrones, which are curves in the Hertzsprung-Russell diagram that depict the evolution of stars of different ages and compositions. However, this method is more suitable for dating stellar clusters since the distance is also required and it is also biased against stars still on the main sequence. On the other hand, the chromospheric technique is calculated based on a star's chromospheric, a region of a star's atmosphere, emissions. This method does not depend on distance and can age stars on the main sequence but it has very large uncertainties.

Unlike these methods, gyrochronology provides a more straightforward and reliable means of age estimation.

3.6 Results

With TESS data available for the majority of the studied targets, we were able to determine rotation periods for a respectable fraction of them with the specific values and percentages shown in Table 3.2. Table 3.2 splits the measured periods into confident and questionable periods.

Table 3.2: Summary of key outcomes of the project, including the number of target stars with data, the rotation periods measured, and gyrochronological ages estimated.

	Totals	Percentages
Total Targets	164	100.0%
Have TESS Data	150	91.5%
Confident Periods	28	17.1%
Questionable Periods	7	4.3%
Measured Gyro Age	20	12.2%

Several periods were considered questionable because of the inability to confirm findings in other sectors or previously published works but the target still had very distinct and clear light curves. Some of these targets may have been seen in additional sectors but those sectors were considered poor. The sectors either were missing data for a sizable amount of days, skewed due to instrumental effects, or affected by oversaturation from stray light from the Moon. The periods that were considered confident had at least one other method or sector that confirmed the original findings.

Figure 3.7 shows the relationship between the measured periods and the temperature of the star. Generally, cooler stars have longer rotation periods compared to hotter stars. This relationship is attributed to the fact that cooler stars have deeper convective zones, which can generate stronger magnetic fields and more efficient magnetic braking. Figure 3.7 does agree with this process.

However, out of the original 164 targets, only 20 of them were able to be age-dated. Figure 3.8 shows the age-related to the temperature of these 20 targets. The correlation between stellar age and temperature is more complex than the relationship between stellar rotation and temperature. The relationship between age and temperature also depends on various factors such as the star’s mass, evolutionary stage, and environment (presence of companions for example). Figure 3.8 does have a slight downward trend suggesting that the cooler stars are much younger. But more age-dated targets are needed before making an in-depth analysis of the trends.

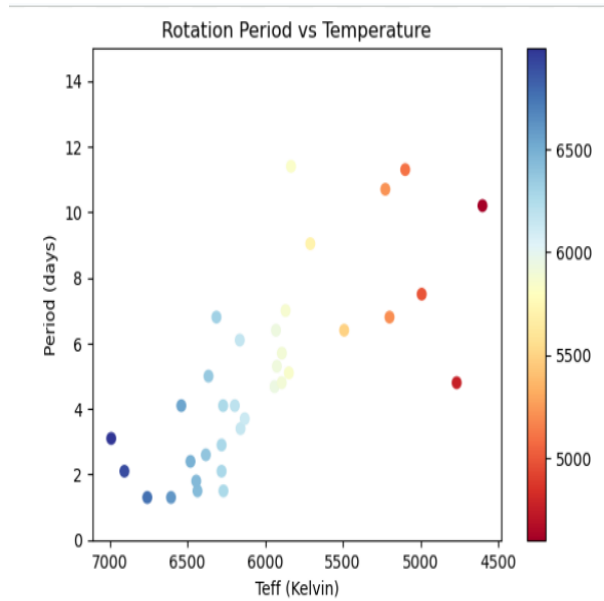


Figure 3.7 Scatter plot showing the relationship between rotation period and effective temperature for the analyzed target stars.

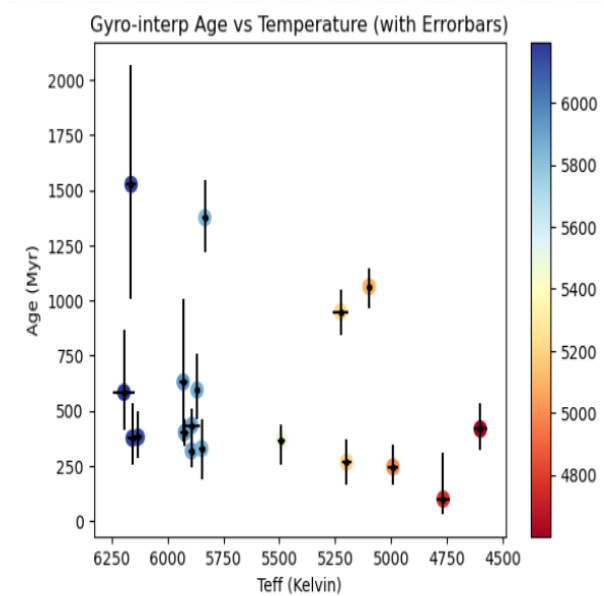


Figure 3.8 Scatter plot showing the relationship between gyrochronology ages and effective temperature for the analyzed target stars.

We identified periods for 35 targets, with the majority corroborated by existing literature. Any uncertainty arises due to incomplete or missing data, instrumental effects, and oversaturation from stray light. In conclusion, only 20 of these targets could be precisely age-dated from the identified periods. Thus resulting in 57% of the targets with determined periods having assigned ages.

Chapter 4

Discussion And Future Work

4.1 Discussion

The ages measured from the target list span from 99 to 1,527 million years (Myr) old. In comparison, the Sun is approximately 4.603 billion years (4603 Myr) old. Thus the age-dated targets are very young stars. Young stars are known to exhibit intense stellar activity, such as frequent flares and strong X-ray emissions, which may pose significant challenges to the development and habitability of life on orbiting planets. If we were to compare the Sun's age to that of the target stars, it would place Earth in the Hadean era or the Archean eon. The Hadean era is characterized by the gradual accumulation of dust and gases, followed by the frequent collisions of larger planetesimals (Johnson et al., 2021). Over time, this process led to the stabilization of Earth's core and crust, marking the initial stages of its development. This led the Earth's atmosphere and oceans to take shape. During the Archean eon, Earth experienced high temperatures, volcanic activity, and the presence of vast oceans. This led to significant geological and atmospheric changes, including the formation of the earliest continents, the emergence of life in the form of single-celled organisms, and the development of oxygen-producing photosynthesis (Johnson et al., 2021). Hence any potential exoplanets around these young stars would also be very young. The Archean eon ranged from approximately 4,000 million years ago - 2,500 million years ago or when the Sun was about 600 million years old to 2,100 million years old. The oldest among our age-dated targets could theoretically host single-celled organisms but this is very optimistic. Ultimately, these stars are far too young to be considered habitable for humanity.

4.2 Future Work

Hence, the primary challenge in identifying more habitable systems lies in detecting longer rotation periods, which typically correspond to older stars. The methods chosen for this project are greatly biased towards younger stars. Since a single sector of TESS observes a target for only 27 days, it is very difficult to detect a rotation period greater than 13 days within a single sector. Attempting to stitch together multiple sectors to overcome this limitation proved to be quite challenging. Many sectors were too widely spaced in time, resulting in difficulties for the model to effectively compare them. And that is if the target had multiple sectors in the first place. On the other hand, several stars had multiple sectors of TESS data but lacked enough activity to be picked up in either analysis method. For instance, Delta Eridani, a naked eye star, is included in the target list and has data in two sectors but has a published rotation period of 158 days (Hemplemann 2016). There is no way to detect a rotation period this large with our current methods.

Therefore the next step is to explore methods that aid in the detection of longer periods. While examining alternative datasets remains an option, we must adopt a more discerning approach in selecting datasets that align closely with our objectives. Although the ASAS-SN dataset contains a wealth of information, our targets often did not correspond to the specific objects the survey primarily focuses on. Alternatively, we can look into other software packages designed to manipulate TESS data. However, it is important to anticipate that this continued exploration of TESS data may yield similar limitations to those encountered in this project.

4.3 Conclusion

In conclusion, this study aimed to contribute to the precursor science efforts for the Habitable Worlds Observatory (HWO) by analyzing rotation periods and estimating gyrochronological ages for a selection of Sun-like stars from the NASA ExEP Mission Star List. Utilizing time-series photometry data from the TESS mission, rotation periods were determined for 21.4 % of the target stars, with gyrochronological ages estimated for 12.2% of the total target star list. 57% of the targets with determined periods were able to be age-dated. The obtained ages ranged from 99 to 1527 million years, showcasing the youthfulness of the sample. As expected, the results were biased towards younger, more

active stars. Moving forward, the focus will be on identifying longer rotation periods, corresponding to older stars, to provide a more balanced understanding of stellar populations and their potential habitability. These findings not only contribute to the ongoing preparatory science for HWO but also highlight the importance of continued exploration and analysis in our quest to understand exoplanetary systems and their potential for harboring life.

References

- (1) Astropy Collaboration et al. *The Astronomical Journal* **2018**, *156* 123, 123.
- (2) Astropy Collaboration et al. *Astronomy and Astrophysics* **2013**, *558* A33, A33.
- (3) Hunter, J. D. *Computing in Science and Engineering* **2007**, *9*, 90–95.
- (4) Lightkurve Collaboration et al. Lightkurve: Kepler and TESS time series analysis in Python, Astrophysics Source Code Library, record ascl:1812.013, 2018.
- (5) Kluyver, T.; Ragan-Kelley, B.; Pérez, F.; Granger, B.; Bussonnier, M.; Frederic, J.; Kelley, K.; Hamrick, J.; Grout, J.; Corlay, S.; Ivanov, P.; Avila, D.; Abdalla, S.; Willing, C.; Jupyter Development Team In *IOS Press*, 2016, pp 87–90.
- (6) Schmitt, J. H. M. M.; Mittag, M. *Astronomische Nachrichten* **2020**, *341*, 497–507.
- (7) Hempelmann, A.; Mittag, M.; Gonzalez-Perez, J. N.; Schmitt, J. H. M. M.; Schröder, K. P.; Rauw, G. *Astronomy and Astrophysics* **2016**, *586* A14, A14.
- (8) Noyes, R. W.; Hartmann, L. W.; Baliunas, S. L.; Duncan, D. K.; Vaughan, A. H. *The Astrophysical Journal* **1984**, *279*, 763–777.
- (9) Baliunas, S.; Sokoloff, D.; Soon, W. *The Astrophysical Journal* **1996**, *457*, L99.
- (10) Baliunas, S. L.; Henry, G. W.; Donahue, R. A.; Fekel, F. C.; Soon, W. H. *The Astrophysical Journal* **1997**, *474*, L119–L122.
- (11) Donahue, R. A.; Saar, S. H.; Baliunas, S. L. *The Astrophysical Journal* **1996**, *466*, 384.
- (12) Egeland, R.; Metcalfe, T. S.; Hall, J. C.; Henry, G. W. *The Astrophysical Journal* **2015**, *812* 12, 12.
- (13) Fetherolf, T.; Pepper, J.; Simpson, E.; Kane, S. R.; Močnik, T.; English, J. E.; Antoci, V.; Huber, D.; Jenkins, J. M.; Stassun, K.; Twicken, J. D.; Vanderspek, R.; Winn, J. N. *The Astrophysical Journal Supplement Series* **2023**, *268* 4, 4.

-
- (14) Dumusque, X.; Pepe, F.; Lovis, C.; Ségransan, D.; Sahlmann, J.; Benz, W.; Bouchy, F.; Mayor, M.; Queloz, D.; Santos, N.; Udry, S. *Nature* **2012**, *491*, 207–211.
- (15) Bazot, M.; Bouchy, F.; Kjeldsen, H.; Charpinet, S.; Laymand, M.; Vauclair, S. *Astronomy and Astrophysics* **2007**, *470*, 295–302.
- (16) DeWarf, L. E.; Datin, K. M.; Guinan, E. F. *The Astrophysical Journal* **2010**, *722*, 343–357.
- (17) Gaidos, E. J.; Henry, G. W.; Henry, S. M. *The Astronomical Journal* **2000**, *120*, 1006–1013.
- (18) Henry, G. W.; Baliunas, S. L.; Donahue, R. A.; Fekel, F. C.; Soon, W. *The Astrophysical Journal* **2000**, *531*, 415–437.
- (19) Suárez Mascareño, A.; Rebolo, R.; González Hernández, J. I.; Esposito, M. *Monthly Notices of the Royal Astronomical Society* **2017**, *468*, 4772–4781.
- (20) Torres, C. A. O.; Ferraz Mello, S. *Astronomy and Astrophysics* **1973**, *27*, 231.
- (21) Watson, C. L.; Henden, A. A.; Price, A. *Society for Astronomical Sciences Annual Symposium* **2006**, *25*, 47.
- (22) Wright, N. J.; Drake, J. J.; Mamajek, E. E.; Henry, G. W. *The Astrophysical Journal* **2011**, *743* 48, 48.
- (23) Abt, H. A. *The Astrophysical Journal Supplement Series* **2009**, *180*, 117–118.
- (24) Abt, H. A. *The Astrophysical Journal Supplement Series* **1981**, *45*, 437–456.
- (25) Akeson, R.; Beichman, C.; Kervella, P.; Fomalont, E.; Benedict, G. F. *The Astronomical Journal* **2021**, *162* 14, 14.
- (26) Casagrande, L.; Schönrich, R.; Asplund, M.; Cassisi, S.; Ramírez, I.; Meléndez, J.; Bensby, T.; Feltzing, S. *Astronomy and Astrophysics* **2011**, *530* A138, A138.
- (27) Corbally, C. J. *The Astrophysical Journal Supplement Series* **1984**, *55*, 657–677.
- (28) Cowley, A. P. *Publications of the Astronomical Society of the Pacific* **1976**, *88*, 95–110.
- (29) Cowley, A. P.; Hiltner, W. A.; Witt, A. N. *The Astronomical Journal* **1967**, *72*, 1334–1340.

-
- (30) Dieterich, S. B.; Henry, T. J.; Golimowski, D. A.; Krist, J. E.; Tanner, A. M. *The Astronomical Journal* **2012**, *144* 64, 64.
- (31) The HIPPARCOS and TYCHO catalogues. Astrometric and photometric star catalogues derived from the ESA HIPPARCOS Space Astrometry Mission, Vol. 1200, ESA Special Publication, Vol. 1200, 1997.
- (32) Eggenberger, P.; Miglio, A.; Carrier, F.; Fernandes, J.; Santos, N. C. *Astronomy and Astrophysics* **2008**, *482*, 631–638.
- (33) Soubiran, C.; Le Campion, J.-F.; Brouillet, N.; Chemin, L. *Astronomy and Astrophysics* **2016**, *591* A118, A118.
- (34) Gaia Collaboration et al. *Astronomy and Astrophysics* **2018**, *616* A1, A1.
- (35) Gaia Collaboration et al. *Astronomy and Astrophysics* **2023**, *674* A1, A1.
- (36) Gray, D. F. *The Astrophysical Journal* **1984**, *281*, 719–722.
- (37) Gray, R. O.; Corbally, C. J.; Garrison, R. F.; McFadden, M. T.; Bubar, E. J.; McGahee, C. E.; O’Donoghue, A. A.; Knox, E. R. *The Astronomical Journal* **2006**, *132*, 161–170.
- (38) Gray, R. O.; Corbally, C. J.; Garrison, R. F.; McFadden, M. T.; Robinson, P. E. *The Astronomical Journal* **2003**, *126*, 2048–2059.
- (39) Gray, R. O.; Napier, M. G.; Winkler, L. I. *The Astronomical Journal* **2001**, *121*, 2148–2158.
- (40) Hauck, B.; Mermilliod, M. *Astronomy and Astrophysics* **1998**, *129*, 431–433.
- (41) Houk, N.; Cowley, A. P., *University of Michigan Catalogue of two-dimensional spectral types for the HD stars. Volume I. Declinations -90_ to -53_f0*. 1975.
- (42) Keenan, P. C.; McNeil, R. C. *The Astrophysical Journal Supplement Series* **1989**, *71*, 245.
- (43) Kharchenko, N. V. *Kinematika i Fizika Nebesnykh Tel* **2001**, *17*, 409–423.
- (44) Kirkpatrick, J. D.; Henry, T. J.; McCarthy Donald W., J. *The Astrophysical Journal Supplement Series* **1991**, *77*, 417.
- (45) Lee, S. -. *The Astronomical Journal* **1984**, *89*, 702–719.

-
- (46) Mermilliod, J. .-.; Mermilliod, M.; Hauck, B. *Astronomy and Astrophysics* **1997**, *124*, 349–352.
- (47) Mermilliod, J. C. *VizieR Online Data Catalog* **1997**, II/168, II/168.
- (48) Montes, D.; González-Peinado, R.; Tabernero, H. M.; Caballero, J. A.; Marfil, E.; Alonso-Floriano, F. J.; Cortés-Contreras, M.; González Hernández, J. I.; Klutsch, A.; Moreno-Jódar, C. *Monthly Notices of the Royal Astronomical Society* **2018**, *479*, 1332–1382.
- (49) Morgan, W. W.; Keenan, P. C. *Annual Review of Astronomy and Astrophysics* **1973**, *11*, 29.
- (50) Newton, E. R.; Charbonneau, D.; Irwin, J.; Mann, A. W. *The Astrophysical Journal* **2015**, *800* 85, 85.
- (51) Ramírez, I.; Allende Prieto, C.; Lambert, D. L. *The Astrophysical Journal* **2013**, *764* 78, 78.
- (52) Schweitzer, A. et al. *Astronomy and Astrophysics* **2019**, *625* A68, A68.
- (53) Soubiran, C.; Brouillet, N.; Casamiquela, L. *Astronomy and Astrophysics* **2022**, *663* A4, A4.
- (54) Stassun, K. G. et al. *The Astronomical Journal* **2019**, *158* 138, 138.
- (55) Takeda, Y.; Ohkubo, M.; Sato, B.; Kambe, E.; Sadakane, K. *Publications of the Astronomical Society of Japan* **2005**, *57*, 27–43.
- (56) Torres, C. A. O.; Quast, G. R.; da Silva, L.; de La Reza, R.; Melo, C. H. F.; Sterzik, M. *Astronomy and Astrophysics* **2006**, *460*, 695–708.
- (57) Twarog, B. A.; Anthony-Twarog, B. J. *The Astronomical Journal* **1995**, *109*, 2828.
- (58) Valenti, J. A.; Fischer, D. A. *The Astrophysical Journal Supplement Series* **2005**, *159*, 141–166.
- (59) van Leeuwen, F. *Astronomy and Astrophysics* **2007**, *474*, 653–664.
- (60) Woolf, V. M.; Wallerstein, G. *Monthly Notices of the Royal Astronomical Society* **2005**, *356*, 963–968.
- (61) Zorec, J.; Royer, F. *Astronomy and Astrophysics* **2012**, *537* A120, A120.

-
- (62) Bouma, L. G.; Palumbo, E. K.; Hillenbrand, L. A. gyointerp: Gyrochronology via interpolation of open cluster rotation sequences, Astrophysics Source Code Library, record ascl:2307.026, 2023.
- (63) Perryman, M. A. C., *The Exoplanet Handbook*; Cambridge, UK ; New York, Cambridge University Press: 2018.
- (64) Bozza, V.; Mancini, L.; Sozzetti, A., *Methods of Detecting Exoplanets*; Springer International Publishing Switzerland: 2016.
- (65) National Academies of Sciences, E.; Medicine, *Pathways to Discovery in Astronomy and Astrophysics for the 2020s*; The National Academies Press: Washington, DC, 2023.
- (66) Ricker, G. R. et al. *Journal of Astronomical Telescopes, Instruments, and Systems* **2014**, *1*, 014003.
- (67) Holcomb, R. J.; Robertson, P.; Hartigan, P.; Oelkers, R. J.; Robinson, C. *The Astrophysical Journal* **2022**, *936*, 138.
- (68) European Southern Observatory: Hertzsprung-Russell Diagram, <https://www.eso.org/public/images/eso0728c/>, Accessed: 2024-03-28.

Chapter 5

Tables

Table 5.1: Published Rotation Periods for HWO Target Stars.

HD ID	TIC ID	P_{rot}	ΔP_{rot}	Ref.
HD 166	TIC 238432056	6.23	...	9
HD 166	TIC 238432056	6.46	...	8
HD 1581	TIC 425935521	15.7	0.1	14
HD 3651	TIC 434210589	44	...	1
HD 4628	TIC 257393898	38.50	...	5
HD 4813	TIC 3962869	4.53	...	8
HD 10476	TIC 113710966	35.20	...	5
HD 10700	TIC 419015728	34	...	1
HD 10780	TIC 373694425	23	...	1
HD 17206	TIC 326242565	3.85	0.01	10
HD 17925	TIC 30016911	6.76	...	5
HD 20010 A	TIC 88523071	4.23	...	8
HD 20630	TIC 343813545	9.00	0.02	10
HD 20630	TIC 343813545	9.24	...	5
HD 22049	TIC 118572803	11.04	...	8
HD 22049	TIC 118572803	11.68	...	5
HD 22049	TIC 118572803	11.76	0.08	10
HD 23249	TIC 38511251	158	13	10
HD 23249	TIC 38511251	3.13	...	8

HD 25457	TIC 9150015	3.02	...	8
HD 25457	TIC 9150015	3.13	...	17
HD 25998	TIC 353257675	2.6	...	12
HD 25998	TIC 353257675	2.72	...	8
HD 25998	TIC 353257675	3.05	...	16
HD 26965	TIC 67772871	43	...	1
HD 30495	TIC 117979951	10.5	0.1	14
HD 30495	TIC 117979951	11	...	1
HD 30495	TIC 117979951	11.36	0.17	7
HD 30495	TIC 117979951	11.83	0.09	10
HD 30495	TIC 117979951	6.06	...	8
HD 30652	TIC 399665349	0.94	...	8
HD 32923	TIC 27136704	32.0	...	13
HD 33262	TIC 381949122	3.51	...	8
HD 35296	TIC 47346402	3.50	0.01	10
HD 35296	TIC 47346402	3.56	...	5
HD 37394	TIC 311063391	10.74	0.03	10
HD 37394	TIC 311063391	11	...	1
HD 37394	TIC 311063391	5.54	...	8
HD 38393	TIC 93280676	6.32	...	8
HD 38858	TIC 176521059	48.0	...	13
HD 43386	TIC 437886584	1.09	...	8
HD 58855	TIC 328324648	16.27	0.21	10
HD 72905	TIC 417762326	4.69	...	5
HD 72905	TIC 417762326	4.85	...	8
HD 72905	TIC 417762326	5.23	0.02	10
HD 74576	TIC 181273463	7.64	...	8
HD 75732	TIC 332064670	39	3	11
HD 75732	TIC 332064670	40.70	0.70	10
HD 75732	TIC 332064670	41.7	1.2	2
HD 76151	TIC 62569281	15	...	1
HD 78154	TIC 219709102	4.67	...	8

HD 78366	TIC 355127594	4.88	...	8
HD 78366	TIC 355127594	9.67	...	5
HD 82885	TIC 8915802	18.60	...	5
HD 84117	TIC 11310083	0.75	...	8
HD 84117	TIC 11310083	5.97	0.03	10
HD 84737	TIC 23969522	4.30	0.02	10
HD 84737	TIC 23969522	40.5	...	13
HD 86728	TIC 172954294	10.64	0.14	10
HD 86728	TIC 172954294	23.0	...	13
HD 90089	TIC 367631379	1.36	...	8
HD 90589	TIC 453620177	0.89	...	8
HD 91324	TIC 447823435	3.15	...	8
HD 95128	TIC 21535479	24.8	0.8	10
HD 95735	TIC 166646191	53	...	1
HD 100623	TIC 57611256	27.5	0.5	10
HD 101501	TIC 101641846	16.68	...	5
HD 103095	TIC 309599261	31	...	1
HD 103095	TIC 309599261	9.90	...	8
HD 105452	TIC 421189312	3.35	...	8
HD 109085	TIC 1628071	0.52	...	8
HD 114710	TIC 445070560	12.35	...	5
HD 115404 A	TIC 373765355	18.47	...	5
HD 115617	TIC 422478973	29	...	1
HD 126660	TIC 441709021	2.87	...	8
HD 128167	TIC 157966796	2.07	...	8
HD 128620	TIC 471011145	22.5	5.9	3
HD 128620	TIC 471011145	36.66	0.30	6
HD 128621	TIC 471011144	31.2	0.7	14
HD 128621	TIC 471011144	36.23	1.36	4
HD 131156 A	TIC 1101124558	6.30	0.04	10
HD 131156 A	TIC 1101124558	6.31	...	5
HD 131156 B	TIC 1101124559	11.94	...	5

HD 131977	TIC 287157634	33.1	0.5	10
HD 134083	TIC 229902025	1.52	...	8
HD 140538	TIC 459427073	21.2	...	13
HD 141004	TIC 296740796	25.80	...	5
HD 143761	TIC 458494003	14.8	...	13
HD 143761	TIC 458494003	17	...	1
HD 146233	TIC 135656809	20.0	...	13
HD 147513	TIC 350673608	6.10	...	8
HD 149661	TIC 58092025	21.07	...	5
HD 155885	TIC 1277142190	21.11	...	5
HD 155886	TIC 1277142191	20.69	...	5
HD 156026	TIC 79841001	21	...	1
HD 156274	TIC 217157387	1.37	...	8
HD 165185	TIC 329574145	5.97	...	8
HD 165341 B	TIC 398120047	20	...	1
HD 166620	TIC 75946144	42.40	...	5
HD 182572	TIC 359981217	41	...	1
HD 185144	TIC 259237827	27	...	1
HD 193664	TIC 403585118	5.62	...	8
HD 197692	TIC 269995013	4.93	...	8
HD 199260	TIC 29495621	4.14	...	8
HD 201091	TIC 165602000	34.1	0.3	10
HD 201091	TIC 165602000	35.37	...	5
HD 201092	TIC 165602023	37.84	...	5
HD 206860	TIC 301880196	4.86	...	5
HD 209100	TIC 231698181	10.58	...	8
HD 209100	TIC 231698181	24.9	0.1	14
HD 210302	TIC 97402436	2.39	...	8
HD 213845	TIC 69889261	1.27	...	8
HD 216803	TIC 206686962	10	...	15
HD 216803	TIC 206686962	10.18	...	8
HD 219482	TIC 234968549	2.17	...	8

Table 5.1: (1) Baliunas et al. [9], (2) Baliunas et al. [10], (3) Bazot et al. [15], (4) DeWarf et al. [16], (5) Donahue et al. [11], (6) Dumusque et al. [14], (7) Egeland et al. [12], (8) Fetherolf et al. [13], (9) Gaidos et al. [17], (10) Hempelmann et al. [7], (11) Hempelmann et al. [7], (12) Hempelmann et al. [7], (13) Henry et al. [18], (14) Noyes et al. [8], (15) Schmitt and Mittag [6], (16) Suárez Mascareño et al. [19], (17) Torres and Ferraz Mello [20], (18) Watson et al. [21], (19) Wright et al. [22].

Table 5.2: Input Catalog of HWO Target Stars

HD ID	TIC ID	α_{ICRS} (deg)	δ_{ICRS} (deg)	ϖ (mas)	Ref. ...	V (mag)	Ref. ...	Spec. Type ...	Ref. ...	T_{eff} (K)	Ref. ...
166	238432056	1.65326670	29.02150353	72.6419 ± 0.0292	39	6.093	15	G8V	19	5491 ± 18	38
693	289673491	2.81607516	-15.46797792	52.9489 ± 0.0958	39	4.895	14	F8V Fe-0.8 CH-0.5	24	6190 ± 13	38
739	70847587	2.93342115	-35.13311471	46.0425 ± 0.0961	39	5.241	15	F5V	24	6495 ± 85	31
1581	425935521	5.01774431	-64.87479366	116.1826 ± 0.1334	39	4.223	15	F9.5V	24	5932 ± 12	38
2151	267211065	6.43779316	-77.25424612	134.0700 ± 0.1100	25	2.820	13	G0V	24	5806 ± 18	38
3651	434210589	9.84085580	21.25047581	90.0248 ± 0.0482	39	5.863	15	K0.5V	9	5203 ± 23	38
4391	80431620	11.43997054	-47.55198407	66.4509 ± 0.0446	39	5.795	15	G5V Fe-0.8 CH-1	24	5887 ± 33	38
4628	257393898	12.09573323	5.28061375	134.4948 ± 0.0578	39	5.729	15	K2V	19	5007 ± 20	38
4614 A	445258206	12.27622748	57.81517729	199.6080 ± 0.1208	39	3.444	12	F9V	9	5907 ± 12	38
4813	3962869	12.53162068	-10.64432885	62.8022 ± 0.0951	39	5.176	15	F7V	19	6208 ± 15	38
5015	285544488	13.26748516	61.12397204	53.1896 ± 0.1273	33	4.800	13	F8V	17	6105 ± 23	38
7570	229092427	18.79633928	-45.53166461	65.5270 ± 0.0704	39	4.966	15	F9V Fe+0.4	24	6110 ± 12	38
7788 A	52194638	18.94203793	-68.87594481	42.9912 ± 1.0581	39	4.912	18	F5V	24	6436 ± 5	39
9826	189576919	24.19933977	41.40545871	74.1200 ± 0.1900	25	4.100	13	F8V	17	6154 ± 10	38
10361	231005052	24.94818630	-56.19644811	122.0035 ± 0.0319	39	5.876	11	K2V	24	5111 ± 34	38
10360	231005905	24.94921957	-56.19331786	122.1088 ± 0.0365	39	5.764	11	K2V	24	5025 ± 21	38
10647	229137615	25.62214382	-53.74083096	57.6409 ± 0.0453	39	5.520	13	F9V	9	6155 ± 17	38

Table 5.2 continued from previous page

HD	TIC	α_{ICRS}	δ_{ICRS}	ϖ	Ref.	V	Ref.	Spec. Type	Ref.	T_{eff}	Ref.
10476	113710966	25.62401052	20.26851268	130.8234 ± 0.1532	39	5.241	15	K1V	9	5204 ± 11	38
10700	419015728	26.01701307	-15.93747989	273.8097 ± 0.1701	39	3.496	15	G8V	9	5356 ± 11	38
10780	373694425	26.93681015	63.85250306	99.5902 ± 0.0438	39	5.626	15	G9V	19	5358 ± 11	38
14412	72748794	34.74376992	-25.94568716	77.9140 ± 0.0295	39	6.336	15	G8V	24	5401 ± 14	38
17051	166853853	40.63944445	-50.80029309	57.6131 ± 0.0383	39	5.395	15	F9V Fe+0.3	24	6157 ± 18	38
16895	302158903	41.04994423	49.22844852	89.6850 ± 0.1638	39	4.100	13	F7V	17	6263 ± 67	38
17206	326242565	41.27582834	-18.57262283	70.0459 ± 0.1599	39	4.465	14	F7V	27	6330 ± 52	38
17925	30016911	43.13386744	-12.76971335	96.5200 ± 0.0258	39	6.038	15	K1.5V(k)	24	5199 ± 20	38
19373	116988032	47.26674709	49.61327835	94.5412 ± 0.1448	39	4.050	13	G0V	9	5952 ± 12	31
20010 A	88523071	48.01887418	-28.98762199	71.4337 ± 0.1320	39	3.800	13	F6V	24	6195 ± 50	38
20766	279649057	49.44234773	-62.57532013	83.0240 ± 0.0438	39	5.513	15	G2IV	9	5710 ± 13	38
20807	279649049	49.55341201	-62.50636242	83.0606 ± 0.0608	39	5.232	15	G1V	9	5847 ± 13	38
20630	343813545	49.84040134	3.37019865	107.8023 ± 0.1838	39	4.850	15	G5V	9	5709 ± 11	38
20794	301051051	49.98187880	-43.06978200	165.5242 ± 0.0784	39	4.258	15	G6V	9	5432 ± 12	38
22001	262843771	52.34448925	-62.93752894	45.9103 ± 0.0934	39	4.703	15	F3V	24	6662 ± 129	36
22049	118572803	53.23268538	-9.45826097	310.5773 ± 0.1355	39	3.718	15	K2V	9	5098 ± 10	38
22484	311092847	54.21826544	0.40166447	71.8370 ± 0.1503	39	4.291	15	F9IV-V	9	5996 ± 9	38
23249	38511251	55.81208557	-9.76339193	110.0254 ± 0.1944	39	3.537	15	K0+IV	9	5045 ± 24	38
23754	121078878	56.71203049	-23.24972280	56.2281 ± 0.1393	39	4.210	15	F5IV-V	24	6685 ± 80	28

Table 5.2 continued from previous page

HD	TIC	α_{ICRS}	δ_{ICRS}	ϖ	Ref.	V	Ref.	Spec. Type	Ref.	T_{eff}	Ref.
25457	9150015	60.65310113	-0.26892220	53.4559 ± 0.0702	39	5.361	15	F7V	19	6268 ± 26	38
25998	353257675	62.15257149	38.03973856	47.1878 ± 0.0734	39	5.522	14	F8V	19	6381 ± 74	38
26965	67772871	63.81799841	-7.65286966	199.6080 ± 0.1208	39	4.415	15	K0.5V	24	5133 ± 43	38
30495	117979951	71.90121543	-16.93445569	75.5289 ± 0.0539	39	5.489	15	G1.5V(n)	24	5833 ± 10	38
30652	399665349	72.46004544	6.96127453	123.9400 ± 0.1700	25	3.184	15	F6V	2	6443 ± 14	38
32147	213041474	75.20416394	-5.75367342	113.0715 ± 0.0222	39	6.202	15	K3+V	19	4810 ± 20	38
33262	381949122	76.37773198	-57.47270469	85.5233 ± 0.0755	39	4.701	15	F9V Fe-0.5	24	6158 ± 23	38
32923	27136704	76.86252320	18.64504994	62.8252 ± 0.1094	39	4.915	15	G1V	19	5691 ± 17	38
34411	409104974	79.78531437	40.09905141	79.6021 ± 0.1005	39	4.705	13	G1.5V	9	5854 ± 13	38
33564	142103211	80.63971084	79.23115073	48.1098 ± 0.0727	39	5.080	13	F7V	19	6354 ± 32	38
35296	47346402	81.10609696	17.38353512	68.5908 ± 0.1040	39	5.009	15	F8V	19	6131 ± 18	38
39091	261136679	84.29119519	-80.46912071	54.6825 ± 0.0354	39	5.666	15	G0V	24	5982 ± 15	38
37394	311063391	85.33473200	53.48105801	81.4987 ± 0.0253	39	6.200	15	K1V	1	5226 ± 36	38
38392	93279196	86.11056968	-22.42183736	112.4661 ± 0.0225	39	6.142	15	K2.5V	24	4950 ± 62	34
38393	93280676	86.11579424	-22.44838549	112.2960 ± 0.1452	39	3.596	15	F6.5V	24	6313 ± 26	38
38858	176521059	87.14558440	-4.09464494	65.7446 ± 0.0307	39	5.973	15	G2V	19	5731 ± 18	38
43834	141810080	92.56030243	-74.75304398	97.9158 ± 0.0573	39	5.076	15	G7V	24	5594 ± 14	38
43042	46125330	93.71198477	19.15644790	45.9214 ± 0.2358	39	5.200	13	F5.5IV-V	19	6539 ± 65	31
43386	437886584	94.11091294	12.27216323	51.0518 ± 0.0969	39	5.040	13	F5V	19	6480 ± 80	16

Table 5.2 continued from previous page

HD	TIC	α_{ICRS}	δ_{ICRS}	ϖ	Ref.	V	Ref.	Spec. Type	Ref.	T_{eff}	Ref.
46588	141523112	101.55895815	79.56481071	54.9380 ± 0.0595	39	5.440	13	F8V	19	6204 ± 23	38
48682	307754027	101.68473723	43.57742456	60.2024 ± 0.0865	39	5.252	15	F9V	19	6066 ± 30	38
50281	282210766	103.07521060	-5.17371267	114.3547 ± 0.0418	39	6.562	15	K3.5V	19	4767 ± 31	38
50692	80226651	103.82777649	25.37569543	57.4559 ± 0.0907	39	5.763	15	G0V	19	5924 ± 17	38
53705	130645536	105.98881342	-43.60803496	58.6192 ± 0.0477	39	5.560	13	G1.5V	9	5790 ± 15	38
55575	156890613	108.95891324	47.23996345	59.3408 ± 0.0535	39	5.559	15	F9V	19	5902 ± 14	38
58855	328324648	112.48315488	49.67245940	49.0145 ± 0.1406	39	5.350	13	F6V	17	6349 ± 25	38
64379	150796339	118.06526236	-34.70543992	54.5631 ± 0.0665	39	5.085	18	F5V Fe-0.5	24	6525 ± 80	28
65907 A	372914091	119.44547625	-60.30307193	61.8360 ± 0.0417	39	5.592	15	F9.5V	24	5997 ± 16	38
69830	307624961	124.59977903	-12.63217144	79.4953 ± 0.0400	39	5.951	15	G8+V	24	5423 ± 9	38
69897	302188141	125.01608650	27.21770505	54.8749 ± 0.0906	39	5.130	13	F6V	19	6269 ± 18	38
72673	393844873	128.21456533	-31.50085138	82.2080 ± 0.0178	39	6.378	15	K1V	9	5261 ± 14	38
72905	417762326	129.79876921	65.02090642	69.2576 ± 0.0485	39	5.630	13	G0.5V Fe-0.5	17	5893 ± 14	38
74576	181273463	130.82512655	-38.88238079	89.3522 ± 0.0151	39	6.556	15	K2.5V(k)	24	4992 ± 22	38
75732	332064670	133.14921294	28.33082083	79.4482 ± 0.0429	39	5.960	13	K0IV-V	19	5292 ± 43	38
76151	62569281	133.57477957	-5.43445953	59.3595 ± 0.0408	39	6.008	15	G2V	9	5780 ± 9	38
78366	355127594	137.21279326	33.88221843	52.7709 ± 0.0309	39	5.962	15	G0IV-V	19	5992 ± 20	38
78154	219709102	137.59811111	67.13401716	48.7404 ± 0.0763	39	4.809	18	F7V	5	6325 ± 42	38
82885	8915802	143.91459247	35.81013251	89.0092 ± 0.0937	39	5.402	15	G9-IV-V Hdel1	9	5518 ± 21	38

Table 5.2 continued from previous page

HD	TIC	α_{ICRS}	δ_{ICRS}	ϖ	Ref.	V	Ref.	Spec. Type	Ref.	T_{eff}	Ref.
84117	11310083	145.56006751	-23.91556723	66.8827 ± 0.1123	39	4.914	15	F9V	9	6163 ± 20	38
84737	23969522	147.14738062	46.02100739	53.1277 ± 0.0773	39	5.086	15	G0(V)	9	5893 ± 13	38
86728	172954294	150.25273698	31.92367028	66.9958 ± 0.0921	39	5.378	15	G4IV	9	5743 ± 14	38
88230	371520835	152.84224979	49.45423639	205.3148 ± 0.0224	39	6.550	15	K7V	10	4097 ± 40	38
89449	95431211	154.93403005	19.47091277	47.1255 ± 0.1679	39	4.792	15	F6IV-V	19	6410 ± 76	33
90589	453620177	156.09877488	-74.03161211	61.6400 ± 0.1200	25	3.990	13	F3V	24	6905 ± 80	28
90839	416519065	157.65658027	55.98053880	77.2485 ± 0.0805	39	4.820	13	F8V	19	6164 ± 21	38
90089	367631379	157.76961635	82.55865174	43.9944 ± 0.2712	33	5.250	13	F4VkF2mF2	19	6758 ± 90	28
91324	447823435	157.84092030	-53.71548361	45.3276 ± 0.0662	39	4.897	15	F9V Fe-0.8 CH-0.7	24	6155 ± 24	38
95128	21535479	164.86655313	40.43025571	72.0070 ± 0.0974	39	5.037	15	G1.5IV-V Fe-1	9	5880 ± 10	38
95735	166646191	165.83414508	35.96988227	392.7529 ± 0.0321	39	7.421	15	M2V	10	3601 ± 51	35
100623	57611256	173.62286018	-32.83133966	104.6133 ± 0.0277	39	5.956	15	K0-V	24	5196 ± 23	38
101501	101641846	175.26256779	34.20163378	104.4252 ± 0.1005	39	5.308	15	G8V	9	5491 ± 24	38
102365	454082369	176.62946889	-40.50035719	107.3024 ± 0.0873	39	4.893	15	G2V	24	5618 ± 14	38
102870	366661076	177.67382715	1.76472265	91.5000 ± 0.2200	25	3.602	15	F9V	2	6123 ± 9	38
103095	309599261	178.24486391	37.71868170	109.0296 ± 0.0197	39	6.427	15	K1V Fe-1.5	19	5057 ± 18	38
105452	421189312	182.10340218	-24.72887510	66.9500 ± 0.1500	25	4.025	15	F1V	24	6990 ± 80	28
109085	1628071	188.01761001	-16.19600517	54.8135 ± 0.1562	39	4.297	15	F2V	24	6871 ± 48	29
109358	458445966	188.43560105	41.35747815	118.0266 ± 0.1530	39	4.260	12	G0V	9	5878 ± 14	38

Table 5.2 continued from previous page

HD	TIC	α_{ICRS}	δ_{ICRS}	ϖ	Ref.	V	Ref.	Spec. Type	Ref.	T_{eff}	Ref.
110897	389853353	191.24752068	39.27891615	56.9588 ± 0.0323	39	5.958	15	F9V Fe-0.3	19	5889 ± 16	38
114710	445070560	197.96830761	27.87818397	108.7250 ± 0.1645	39	4.230	13	F9.5V	9	5996 ± 17	38
114613	30293512	198.01326790	-37.80302220	48.8691 ± 0.1058	39	4.847	15	G4IV	24	5688 ± 14	38
114837	255854921	198.56310307	-59.10323723	54.8247 ± 0.0809	39	4.913	12	F6V Fe-0.4	24	6238 ± 26	38
115404 A	373765355	199.21271429	17.01717803	91.0176 ± 0.0236	39	6.550	13	K2.5V(k)	19	4843 ± 107	38
115617	422478973	199.60130828	-18.31119382	117.1726 ± 0.1456	39	4.735	15	G6.5V	9	5552 ± 9	38
122064	202380743	209.38357650	61.49286115	99.3325 ± 0.0193	39	6.488	18	K3V	6	4867 ± 29	38
125276	83391616	214.75373205	-25.81542495	55.5900 ± 0.0531	39	5.872	15	F9V Fe-1.5 CH-0.7	24	6120 ± 41	38
126660	441709021	216.29915429	51.85074358	68.8200 ± 0.1400	25	4.052	13	F7V	17	6280 ± 16	38
128167	157966796	218.67007244	29.74512713	63.4679 ± 0.1173	39	4.465	15	F4VkF2mF1	17	6745 ± 73	31
128621	471011144	219.89609629	-60.83752757	750.8100 ± 0.3800	37	1.350	13	K1V	3	5244 ± 13	38
128620	471011145	219.90205833	-60.83399269	750.8100 ± 0.3800	37	0.002	12	G2V	24	5776 ± 16	38
131156 B	1101124559	222.84601534	19.10191326	148.1793 ± 0.0546	39	6.979	12	K5V	5	4288 ± 127	36
131156 A	1101124558	222.84745194	19.10044994	148.0695 ± 0.1317	39	4.540	13	G8-V	19	5487 ± 19	38
131977	287157634	224.36666997	-21.41547980	169.8843 ± 0.0653	39	5.724	15	K4V	9	4632 ± 15	38
134083	229902025	226.82527473	24.86919428	51.1875 ± 0.0879	39	4.940	15	F5V	19	6435 ± 44	20
136352	136916387	230.45062463	-48.31763053	67.8467 ± 0.0601	39	5.655	15	G2.5V Hdel1	24	5685 ± 17	38
140538 A	459427073	236.00757737	2.51516683	67.6007 ± 0.0360	39	5.869	15	G5V	17	5682 ± 12	38
141004	296740796	236.61089255	7.35306872	83.9214 ± 0.1501	39	4.422	15	G0-V(k)	9	5898 ± 10	38

Table 5.2 continued from previous page

HD	TIC	α_{ICRS}	δ_{ICRS}	ϖ	Ref.	V	Ref.	Spec. Type	Ref.	T_{eff}	Ref.
140901	179348425	236.87125423	-37.91631192	65.5889 ± 0.0342	39	6.012	15	G7IV-V	24	5602 ± 14	38
142373	157364190	238.16892104	42.45151747	62.9028 ± 0.0807	39	4.608	15	G0V Fe+0.4	19	5820 ± 30	38
142860	377415363	239.11326123	15.66161681	88.8600 ± 0.1800	25	3.843	15	F6V	17	6285 ± 13	38
143761	458494003	240.26108537	33.30351096	57.1076 ± 0.0508	39	5.410	15	G0IV	9	5812 ± 11	38
146233	135656809	243.90529281	-8.36943948	70.7371 ± 0.0631	39	5.496	15	G3+V	9	5785 ± 12	38
147513	350673608	246.00537974	-39.19298053	77.5655 ± 0.0661	39	5.370	15	G1V CH-0.4(k)	24	5868 ± 12	38
149661	58092025	249.08937371	-2.32458695	101.0719 ± 0.0501	39	5.764	15	K0V(k)	24	5262 ± 11	38
155886	1277142191	258.83659854	-26.60169922	168.0031 ± 0.1343	39	5.070	13	K1V	5	5132 ± 26	38
155885	1277142190	258.83743261	-26.60282596	168.1303 ± 0.1081	39	5.110	13	K1V	5	5144 ± 31	38
156026	79841001	259.05567673	-26.54614905	167.9617 ± 0.0311	39	6.295	15	K5V(k)	24	4476 ± 24	38
156274	217157387	259.76598980	-46.63623345	113.7513 ± 0.0726	39	5.472	15	G9V	7	5235 ± 20	38
157214	9728611	260.16486437	32.46774388	68.5575 ± 0.0553	39	5.385	15	G0V	17	5704 ± 13	38
156897	75899957	260.25156050	-21.11293639	57.0820 ± 0.1851	39	4.389	12	F2V	24	6756 ± 80	28
158633	219880402	261.25040726	67.30670798	78.1747 ± 0.0226	39	6.443	15	K0V	1	5302 ± 16	38
160032	96745915	265.09927324	-49.41558313	47.7045 ± 0.1368	39	4.762	12	F4V	8	6620 ± 80	28
160915	238115675	265.85747308	-21.68319414	56.6500 ± 0.2400	25	4.860	13	F5V	24	6404 ± 36	38
160691	362661163	266.03626309	-51.83405322	64.0853 ± 0.0904	39	5.124	15	G3V	24	5761 ± 11	38
165341 A	1674663309	271.36353505	2.50014628	195.5674 ± 0.1964	39	4.220	13	K0-V	9	5298 ± 32	38
165341 B	398120047	271.36442890	2.49894700	195.2166 ± 0.1012	33	6.061	26	K4V	1	4475 ± 33	32

Table 5.2 continued from previous page

HD	TIC	α_{ICRS}	δ_{ICRS}	ϖ	Ref.	V	Ref.	Spec. Type	Ref.	T_{eff}	Ref.
165185	329574145	271.59883133	-36.01978628	58.4296 ± 0.0404	39	5.949	15	G0V	24	5892 ± 36	38
166620	75946144	272.40590088	38.45777723	90.1234 ± 0.0156	39	6.377	15	K2V	19	5028 ± 17	38
165499	303704858	272.60897375	-62.00222005	56.3280 ± 0.1231	33	5.469	15	G0V	24	5951 ± 29	38
168151	233121747	273.47430336	64.39728493	43.1837 ± 0.0940	39	4.990	13	F5V	4	6473 ± 38	38
182572	359981217	291.24249988	11.94441347	67.0153 ± 0.0657	39	5.169	15	G7IV-V	9	5593 ± 19	38
185144	259237827	293.08995921	69.66117661	173.4939 ± 0.0748	39	4.672	15	K0V	9	5298 ± 14	38
187013	58445695	296.60666687	33.72759820	47.6516 ± 0.0675	39	5.005	15	F5.5IV-V	19	6455 ± 28	22
187691	408842743	297.75684873	10.41572013	51.3133 ± 0.0898	39	5.122	15	F8V	17	6134 ± 12	38
190360	105999792	300.90585453	29.89680345	62.4865 ± 0.0354	39	5.745	15	G7V	24	5563 ± 11	38
189567	352402781	301.38652287	-67.32089615	55.7654 ± 0.0245	39	6.070	13	G2V Fe-1.0	24	5730 ± 15	38
190248	409891396	302.18170363	-66.18206744	163.9544 ± 0.1222	39	3.556	12	G8IV-V	24	5576 ± 17	38
191408	389198736	302.79974487	-36.10120881	166.3272 ± 0.1065	39	5.297	15	K2.5V	24	4980 ± 19	38
192310	326096771	303.82246407	-27.03297545	113.4872 ± 0.0516	39	5.730	15	K2+V	24	5087 ± 11	38
193664	403585118	304.38053380	66.85368902	57.2041 ± 0.0208	39	5.922	15	G0V	19	5930 ± 18	38
197692	269995013	311.52388594	-25.27089754	68.3370 ± 0.1823	39	4.137	15	F5V	24	6638 ± 80	28
199260	29495621	314.19721527	-26.29637787	47.3886 ± 0.0696	39	5.709	15	F6V	24	6270 ± 27	38
201091	165602000	316.72474829	38.74941732	285.9949 ± 0.0599	39	5.211	15	K5V	9	4441 ± 37	38
201092	165602023	316.73026602	38.74204403	286.0054 ± 0.0289	39	6.043	15	K7V	9	4107 ± 51	38
202560	159746875	319.31362112	-38.86736221	251.9124 ± 0.0352	39	6.690	18	M0V	23	$3874 \pm$	40

Table 5.2 continued from previous page

HD	TIC	α_{ICRS}	δ_{ICRS}	ϖ	Ref.	V	Ref.	Spec. Type	Ref.	T_{eff}	Ref.
203608	265488188	321.61085409	-65.36619807	108.0102 ± 0.1061	39	4.229	15	F9V Fe-1.4 CH-0.7	24	6095 ± 24	38
206860	301880196	326.13054144	14.77193980	55.1480 ± 0.0348	39	5.942	12	G0IV-V	19	5939 ± 21	38
207129	147407292	327.06562985	-47.30361608	64.2717 ± 0.0430	39	5.575	15	G0VmF2	24	5935 ± 15	38
209100	231698181	330.84022344	-56.78597855	274.8431 ± 0.0956	39	4.674	15	K4V(k)	24	4641 ± 21	38
210302	97402436	332.53658414	-32.54840842	54.1773 ± 0.0940	39	4.940	13	F6V	24	6364 ± 28	38
212330	259291108	336.23486946	-57.79745589	49.1648 ± 0.1075	39	5.318	15	G2IV-V	24	5660 ± 18	38
213845	69889261	338.67348244	-20.70821581	43.4396 ± 0.0828	39	5.210	13	F5V	24	6605 ± 33	39
215648	60716322	341.67324939	12.17288579	61.9161 ± 0.1739	39	4.200	13	F6V	17	6193 ± 23	38
216803	206686962	344.10021899	-31.56556405	131.5525 ± 0.0275	39	6.446	15	K4Ve	9	4601 ± 29	38
217987	155315739	346.46681577	-35.85307088	304.2190 ± 0.0451	33	7.330	15	M1.0V	30	3680 ± 130	21
219134	283722336	348.32072900	57.16835662	152.8640 ± 0.0494	39	5.540	15	K3V	9	4874 ± 28	38
219623	24467943	349.17626483	53.21347482	48.5197 ± 0.0463	39	5.580	13	F8V	17	6084 ± 24	38
219482	234968549	349.24036453	-62.00119780	48.9174 ± 0.0356	39	5.655	15	F6V	24	6280 ± 31	38
222368	419919445	354.98767240	5.62629098	72.9200 ± 0.1500	25	4.132	15	F7V	17	6200 ± 15	38